UNIVERSITÀ DEGLI STUDI DI MODENA E REGGIO EMILIA

Dipartimento di Scienze Fisiche, Informatiche e Matematiche

Corso di Laurea in Physics

# Electron Phase Microscopy of FeCo Magnetic Nanoparticles

**Relatore:**
Prof. Marco Beleggia

**Correlatore:**
Dott. Paolo Rosi

**Tesi di Laurea di:**
Federico Zanni

Anno Accademico 2024 – 2025

# Electron Phase Microscopy of FeCo Magnetic Nanoparticles

FEDERICO ZANNI

# Abstract

Magnetic properties of nanoscale materials are of fundamental interest for both basic research and technological applications. However, the quantitative magnetic characterization at the nanometer scale is experimentally challenging due to the extreme requirements in terms of spatial resolution and sensitivity to small magnetic fields. Transmission Electron Microscope (TEM) is a powerful tool for the structural and physical characterization of materials at the micro and nanoscale. A TEM technique called off-axis electron holography provides us with the unique opportunity of measuring the elusive phase of the electron wave after interactions with a specimen. This enables the quantitative investigation of the local electric and magnetic properties of nanoscale materials. Electron holography is applied to study the magnetic properties of $Fe_xCo_yO_z$ nanoparticles and nanochains, revealing distinct magnetic responses. Holograms encode the phase modulation of the electron wave function through an interference pattern established by the action of an electron biprism. This phase information, related to electric and magnetic potentials, is then extracted from the data with a well-established FFT based algorithm. After separating the electric and magnetic contributions to the phase, we evaluate the magnetic moment of the nanoparticles, or the flux carried by nanochains with data analysis supported by modelling and image simulations. The comparison between experimental and simulated data shows good agreement, provides important information about the investigated nanostructures and allows a better qualitative and quantitative magnetic characterization of their properties.

# Contents

# Introduction

Magnetism is a subject which has been studied for nearly three thousand years. Lodestone, an iron ore, first attracted the attention of Greek scholars and philosophers, and the navigational magnetic compass was the first technological product resulting from this study. Century after century, the understanding of magnetism has progressed steadily, with a significant acceleration in the past two thousand years, leading to the realization that magnetic phenomena are intrinsically connected with other fundamental physical interactions [1].

Magnetic interactions lie at the heart of this work and, more generally at the core of the Transmission Electron Microscope (TEM). The exceptional resolving power of TEM, extending to the sub-nanometers regime and ultimately to the atomic scale, relies fundamentally on electromagnetic lenses. Without such elements, achieving its extreme resolution level would not be possible. As a consequence, TEM has become a fundamental instrument for the investigation of materials at the nanoscale, providing simultaneous access to structural and chemical information with outstanding spatial resolution [2]. Owing to these properties and capabilities, TEM has opened access to the exploration of nanomaterials, in which reduced dimensions give rise to important and innovative properties. In recent years, this field has undergone rapid development, driven by the design and fabrication of nanostructures: materials with characteristic dimensions in the nanometer range. At these length scales, materials often exhibit remarkable and unconventional electronic and magnetic behaviors [3].

In this context, magnetic nanomaterials are of particular interest for the present work. They have emerged as a pivotal innovation in nanotechnology, gaining substantial attention in view of a wide range of applications, especially in the biomedical fields as well as in other areas of research. Notably, their intrinsic magnetic properties enable controlled self-assembly, leading to the formation of complex structures such as nanoparticle clusters and one dimensional nanochains with specific geometries and functionalities [4].

In this work magnetic iron-cobalt (FeCo) nanoparticles and nanochains are investigated to characterize their magnetic behavior. These nanostructures are of significant technological interest, with applications as contrast agents in magnetic resonance imaging (MRI) [5], in magnetic heating and magnetic hypertermia [6] and more broadly in biomedicine [7, 8]. Furthermore, they are relevant for magnetic data storage [9], electromagnetic wave absorption and microwave shielding [10] and in flexible devices and sensors technologies [11].

A fundamental understanding of these systems requires a detailed characterization of their magnetic properties at the nanoscale, which remains a challenging task. Addressing this problem requires a rigorous description of the interaction between the electron beam and the sample electromagnetic fields within the TEM. In this regard, quantum mechanics provides the essential framework: electrons can be described as coherent waves whose phase encodes information about both electric and magnetic fields within the studied material.

This quantum mechanical and fundamental effect finds its experimental realization in phase-sensitive microscopy techniques and in particular in off-axis electron holography. This method, implemented in this work, enables the retrieval of the phase modulation of the electron wavefront, overcoming the well-known phase problem, and providing us with quantitative reconstruction of electrostatic and magnetic fields. In this way, it provides direct access to the fundamental properties of magnetic nanostructures at the nanoscale.

Finally, the interpretation of such complex interactions necessitates support by numerical simulations. These provide essential references and offer critical insights into the experimental observations, allowing a deeper understanding of the interplay between theoretical models and the complex magnetic nanoscale world.

# *Chapter 1*

# Electron Microscopy

Electrons may be employed as highly sensitive probes to extract information from materials, providing imaging capabilities with resolution beyond those achievable with light. This chapter presents the fundamental reasons and potentials of electron microscopy as a tool for investigating matter at micro- and nanoscale. It introduces the nature of electrons and their interactions with matter. The chapter then describes the main components of a transmission electron microscope, including the generation of the electron beam, the electron optics, the different imaging modes and the signal detection systems. Finally, it outlines the types of specimens that can be analyzed and the kinds of information and properties that can be obtained from specific analyses of them. Together, these concepts provide the fundamental basis for the theoretical and experimental topics discussed in the rest of this work.

## 1.1 Why use electrons in microscopy?

Historically, electron microscopes were developed to overcome the spatial resolution limitations of light microscopes. Electrons, when accelerated by high voltages, reach an extremely small wavelength $\lambda$, described by the de Broglie wavelength, in the order of the picometer ( $\sim 2$ pm for a 300 kV source). This small value, according to the Rayleigh criterion $d = 0.61\frac{\lambda}{NA}$ with $NA$ being the numerical aperture, enables resolving objects of the same size $d$ and with a much higher spatial resolution than that achievable with light-based microscopes. In this way, electrons can be used to observe and investigate materials at the nanometer and even atomic scale. Furthermore, electrons strongly interact with matter and, unlike photons, they are sensitive to electric and magnetic fields. Through these interactions, a wide range of information can be extracted, allowing investigation of materials in terms of their structural, chemical, electronic, magnetic and other fundamental properties over a large range of length scales, from micro to beyond the nanoscale [2].

## 1.2 Electron-matter interactions

Electron microscopy relies on the interaction between an incident electron beam and the system under investigation, from which structural and compositional information can be extracted. When an electron faces a general sample, the interactions happen between the electron (in this approximation considered as a particle, like in a pure Rutherford scattering) and the constitutive atoms of the sample. The interactions are generally classified into two main categories: elastic and inelastic scattering. In elastic scattering electrons interact without losing kinetic energy, changing only their traveling direction. Elastic scattering is one of the major sources of contrast in electron microscopy and is particularly important because it explains and gives rise to the image formation process and to electron diffraction. Another fundamental interaction is inelastic scattering, in which part of the kinetic energy is transferred to the sample, leading to electronic excitations, ionization processes (that can lead to X-rays emissions) or the emission of secondary signals. The energy lost by the electrons in these processes can be measured, providing important information about the material (Electron Energy Loss Spectroscopy - EELS). All the possible interactions between electrons and matter are summarized in Fig. 1.1 [2].

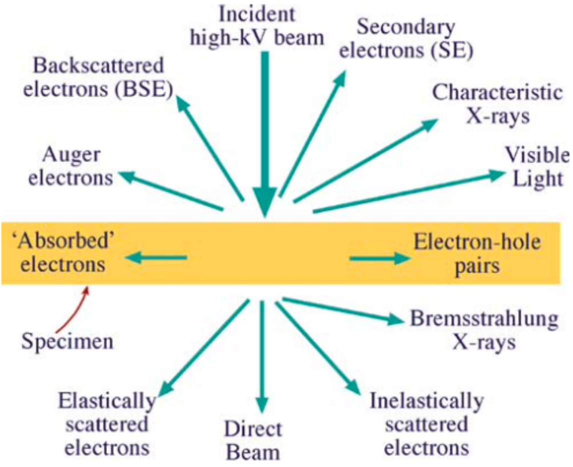

**Figure 1.1:** Signals generated when a high-energy beam of electrons interacts with a thin specimen. The directions shown for each signal do not always represent the physical direction of the signal, but indicate, relatively, where the signal is strongest or where it is detected.

After the interactions, the electron motion is modified and, through the changes in their behavior, it is possible to identify different categories of electrons.

- **Scattered Electrons**: when, after the interaction with atoms, they emerge from the sample with a different angle with respect to the incoming one. The deflection angle depends on the interaction (distance from the nucleus, type of atom and other parameters). In principle, electrons can be scattered in every direction and as mentioned this phenomenon can be elastic or inelastic.

- **Backscattered Electrons**: when, after the interactions, they come back towards the electron source.
- **Unscattered Electrons**: when they cross the sample without relevant interactions. They are exactly the same that are sent on the sample.
- **Secondary Electrons**: electrons that escape from the atoms of the sample after the interaction with the incoming ones. They are the result of energy transfer between moving electrons and electrons inside the clouds around the atoms of the studied system.

These different kinds of electrons can be produced from a single scattering event (first order phenomenon) and from any other higher order of interaction. In general billions of electrons are sent on the sample in small times, therefore a lot of interactions happen together and what emerges from the sample is, in general, the result of a cascade effect. The basic aim of electron microscopy is to collect electrons that have interacted with the sample and use them to obtain information about a wide range of properties of the specimen. Various interactions occur with different probabilities, with most of the electrons going straight through and carrying no information; the percentages and the types of interactions predominantly depend on the nature of the sample and on its thickness.

Over the years, different techniques and microscope configurations have been developed to exploit all these interactions. A major distinction is between Scanning Electron Microscopes (SEMs), which generate images by detecting either backscattered or secondary electrons generated from the surface of the specimen, and Transmission Electron Microscopes (TEMs), which collect electrons transmitted through the sample. In the present work, a TEM is employed to investigate the basic morphological, structural and magnetic properties of the studied materials [12].

## 1.3 The Transmission Electron Microscope

Electrons are excellent probes for the investigation of matter, thanks to their intrinsic properties and to the wide range of interactions they undergo with materials; historically, electron microscopy started with the theory of Louis de Broglie in 1925, describing the electron as a wave-like quantum object [14], with a wavelength smaller than the visible one. A few years later, building on earlier theoretical and experimental work, Max Knoll and Ernst Ruska developed the first prototype of an 'Electron Microscope' and used this name for the first time in a 1932 publication [15], successfully obtaining magnified images using two electron magnetic lenses.

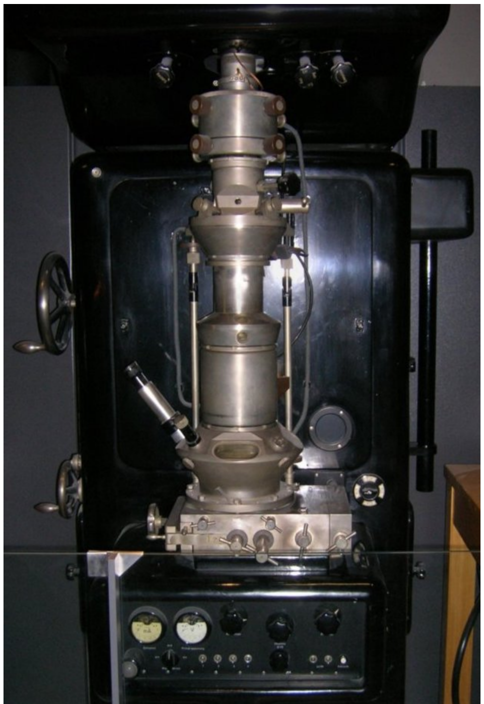

One of the first prototypes of microscope is reported in Fig. 1.2.
In the following years the prototype developed into an imaging device with a resolution limit surpassing that of the light microscope; the Transmission Electron Microscope became a commercial instrument in 1939. The design of the first electron microscope led Ruska to obtain the Nobel Prize in physics in 1986 and the microscope, in the official citation, was described as ‘one of the most important inventions of this century’ [16].

Today, TEMs can be considered the most efficient and versatile tools for characterization of materials over spatial ranges from the atomic scale, through the important ‘nano’ regime (from 1 *nm* to about 100 *nm*), up to micrometer level and beyond. For this reason and for the increasing demand due to the rapid expansion of nanotechnologies, material sciences, and biotechnology, TEM are very widespread throughout the world. It can be estimated from industry statistics that over 8000 TEM are installed globally across research laboratories, universities, semiconductor facilities, and healthcare institutions [17].

In order to correctly interpret electron microscopy images and understand the interaction between electrons and matter, it is necessary to describe how the electron beam is generated, how it propagates through the microscope column and how the resulting signals are collected and analyzed. Therefore, the structure and main components of a transmission electron microscope are introduced in the following subsections.

### 1.3.1 Electron Sources

A performing source (gun) of electrons to illuminate the sample is one of the most important parts of a TEM. The beam of electrons needs to own specific properties in order to enable a good performance of the whole microscope. These characteristics are severe requirements that are strictly related to the type of the employed instrument and to the kind of analysis. The most important properties are brightness, temporal coherence, spatial coherence and stability. Brightness expresses the electron current density per unit of solid angle, hence the amount of electrons produced in time related to the divergence angle of the beam. Temporal coherence (also known as longitudinal coherence) evaluates for how long electrons emitted at different times can maintain a phase relationship with one another and this quantity is strongly connected with the energy spread of the beam and so with the variation in wavelength. On the other hand, spatial coherence (also known as transverse coherence) depends on the size of the source and quantifies how many different electrons can be considered produced from the same point of the source. Finally, another important property is that the electron current coming from the source remains stable, otherwise taking images and making analysis on them becomes impossible. These stringent requirements are best met by only three types of source:

- **Thermoionic Source**
  Electrons are produced by directly heating specific materials, such as a tungsten (W) filament or a lantanium hexaboride ($LaB_6$) crystal, called cathode of the gun. The electrons are then accelerated by high positive voltages ($\sim 10^3$ kV) and converged through the Wehnelt cylinder, a small negatively charged grid that helps to obtain a controllable electron beam through the anode (Fig. 1.3a).
- **Schottky Source**
  Electrons are produced through the Schottky effect, by heating, at lower temperature with respect to thermoionic sources, and by applying a strong electric field that lowers the surface barrier of the material (generally a sharp tip of tungsten (W) covered with zirconium oxide ($ZrO_2$)). Then the voltage between the cathode and an anode accelerates the electrons at the right energy (Fig. 1.3b).
- **Field Emission Source (FEG)**
  Electrons are produced by applying a large electric potential (larger than other sources) between the source and an anode; this leads the electron to tunnel out from the gun (generally a tungsten (W) needle) without heating. A second anode is used to accelerate the electrons at an appropriate energy and controls the source size (Fig. 1.3c).

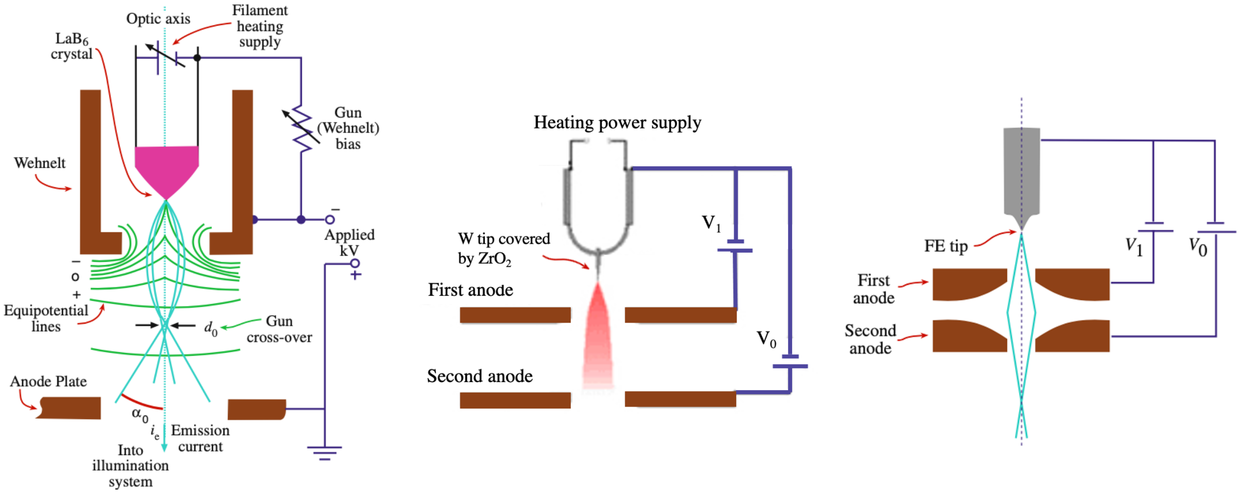

**(a)** **(b)** **(c)**

**Figure 1.3:** Electron Sources: (a) Thermoionic source. (b) Schottky source. (c) Field-Emission source. $V_1$ is the extraction potential, $V_0$ is the anode/accelerating voltage.

All the sources are incorporated into a gun assembly that extracts, accelerates and acts as a lens to focus the produced electrons to form a crossover, which represents the first image of the emitter and operates as the effective electron source for the illumination system. Then the beam passes through a hole in the anode and propagates towards the condenser lens system. Although thermionic and

Schottky sources are robust and relatively simple, FEGs provide significantly higher brightness, smaller virtual source size and reduced energy spread. These characteristics result in improved spatial, temporal coherence and enhanced high-resolution performance. For this reason and thanks to the increased computer control FEG-based TEM instruments are increasingly preferred for advanced applications [2, 12].

### 1.3.2 Electron Lenses

Electron Lenses in a TEM control all the basic operational functions of the instruments. They are equivalent to the glass lenses in a light microscope. In general, the behavior of all the lenses in a standard TEM can be reasonably approximated to the action of a convex glass lens on monochromatic light with a fundamental difference: to change magnification in light microscopy lenses are physically moved, while in electron microscopy the lenses are fixed in position and their effects are controlled by changing their characteristics (generally their strength). This parallelism between optical and electron lenses allows to use ray diagrams and geometric optics equations to represent and describe the basic workings of TEM lenses.

The fundamental aims of electron lenses are to focus and magnify electron beams, images and diffraction patterns (DP) inside the microscope. In order to act on electrons, they are electromagnetic lenses and, in particular, magnetic ones are always the most implemented in the TEM column. Magnetic lenses are made of two parts (shown in the cross section in Fig. 1.4a): the polepiece, a cylindrically symmetrical core of soft magnetic material with a hole (called bore) drilled through it, and a coil of copper wire, which surrounds the polepiece, inducing a magnetic field in the bore when a current flows through the wires. This created magnetic field is axially symmetric and its strength controls the electron trajectories. In most lenses there are two polepieces (upper and lower) separated by a distance called gap. Coils resistive heating can be a problem and lenses need to be cooled by a water recirculating system. The dimensions of the gap and the bore are two important characteristics of a lens that determine its focusing action.

When the electrons enter inside the field created by the lens with their relativistic velocity, they experience Lorentz force and their equation of motion can be evaluated. Working in cylindrical coordinates $(r, \theta, z)$, under paraxial approximation (small $r$ coordinate, small radial velocity $\dot{r}$, small azimuthal velocity $r\dot{\theta}$ and constant velocity along z-axis) and applying Newton's law is possible to extract the two equations that fully describe the behavior of the angular and of the radial electron coordinates:

$$\theta(z) = \theta_0 + \frac{e}{2\sqrt{2mU^*}} \int_{z_0}^{z} B(z)\, dz \tag{1.1}$$

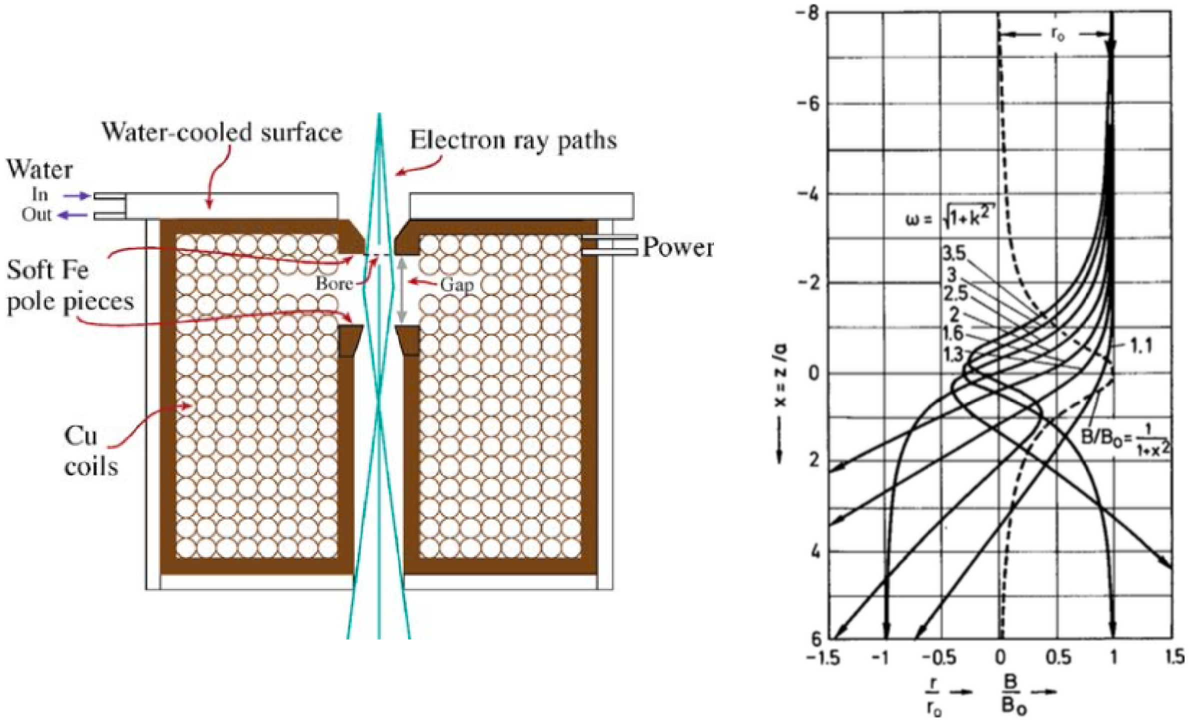

**(a)** **(b)**

**Figure 1.4:** Electron lens: (a) Cross section of a typical magnetic lens. (b) Electron trajectory when passing through a lens with a bell-shaped field, for different lens strengths $\omega$. Stronger lens deviates more the electrons and focuses them faster.

$$\ddot{r}(r,z) = -\frac{e^2}{16mU^*}B^2(z)r \tag{1.2}$$

where $\theta_0, e, m, B(z)$ are, respectively, the initial azimuthal angle (in the reference plane $z = z_0$), the electron charge, the electron mass and the lens magnetic field. $U^*$ is the relativistic corrected electron energy, defined as $U^* = eV_{acc}(1 + \frac{eV_{acc}}{2mc^2})$, with $V_{acc}$ the accelerating electron voltage and $c = 2.998 \times 10^8$ m/s the speed of light. Eq. 1.1 describes the rotation around the z-axis of the electrons through their angular coordinate, while Eq. 1.2 highlights the presence of a radial force that pulls the electrons towards the optical z-axis. Hence, under the paraxial approximation, the combination of a rotation, of the radial focusing due to centripetal acceleration and of an approximately constant axial velocity results in a converging spiral (helical) motion towards the axis. More precisely, this converging motion occurs only if the magnetic field is non-uniform along z-axis, otherwise the electrons would follow a helical trajectory of constant radius and therefore would not converge. In general, the non-uniform field produced by a magnetic lens is represented by a Glaser bell-shaped field:

$$B(z) = \frac{B_0}{1 + (z/a)^2} \tag{1.3}$$

with $B_0$ the maximum and $2a$ the FWHM; the resulting electron trajectory is shown in Fig 1.4b for different strengths of the lens.

These principles are the basis for all the different kinds of lenses used in TEM. The focal length $f$ quantifies the strength of a lens: lenses with short $f$ are called strong lenses while those with larger $f$ are known as weak lenses. The strength of lens is therefore controlled by the magnetic field produced by it; for example, increasing the field (changing the excitation current of the lens) the electrons are more focused towards the axis and the focal length becomes smaller. As shown in Eq. 1.1 and 1.2, the motion of the electrons depends also on their energy $U^*$ (strictly related to their accelerating voltage), hence changing it modifies also the effects of the lenses (electrons with larger momentum are more difficult to bend), but in general this is not a real problem in TEM, where the accelerating voltages are generally fixed. Most lenses in TEM are weak lenses and act to demagnify the source image or to magnify the image or the DP. The most important one is called objective lens, it is very strong, there exist several types of it depending on the needs, and it is fully described in Subsection 1.3.5.

In conventional magnetic lenses the soft iron used in the polepieces presents a saturation magnetization of about 2 T and this can limit the focusing strength. Furthermore, copper coils require high current and present instabilities related to their resistive heating. These limitations of ferromagnetic polepieces can be overcome using superconducting lenses; they present very high magnetic field (several Tesla), no resistive heating, better field stability and very small aberrations, but they require superconducting materials, cryogenic temperatures and high costs. In superconducting lenses the field can be varied only after technically complex operations, therefore they are not continuously and precisely tunable and this is their major practical drawback. There are not only lenses made of one or two polepieces, it is also possible to design quadrupole, sextupole or octupole lenses in which the focusing action is achieved by $4, 6, 8$ adjacent polepieces respectively. These lenses are used to correct lens defects and aberrations.

Electron lenses are not ideal and there are many kinds of lens defects (aberrations) that limit the microscope performance in substantial ways. Imperfections deviate the electron from the ideal focus and, as a result, the image is distorted, blurred or has reduced resolution. Aberrations are generally divided into two main categories: geometrical and chromatic aberrations. Here only major defects in lenses are presented [2, 12]:

**Geometrical Aberrations**

They are related to the geometry of the ray trajectories and arises from imperfections in electron lens imaging, causing deviations from ideal focusing. They can be broadly classified into Seidel aberrations and parasitic aberrations. The parasitic aberrations are real-world defects caused by misalignments, instabilities, imperfections in the microscope and lens non-uniformity; they degrade quality of the images and are particularly critical in High-Resolution imaging. The five classical Seidel aberrations are the following:

- **Spherical aberration**
  This defect occurs when the lens field behaves differently for off-axis rays. In electron lenses, the farther off axis the electron is, the more strongly it is bent back toward the axis (reduced

$f$). As a result, a point object is imaged as a disk of finite size; this, therefore, limits the ability to magnify details because they are degraded by the imaging process. The error $d$ in the image, created by this effect, is quantified by the Spherical Aberrations Coefficient $C_s$ and depends on the third power of the angle $\beta$ between the optical axis and the electron beam ($d \sim C_s\beta^3$). Spherical aberrations limits the resolution of the microscope, producing symmetric blur disks. It can be compensated by creating a diverging effects which spreads out the off-axis beams such that they re-converge to a point; in practice this is achieved by complex and computer controlled set of quadrupoles and hexapoles or octupoles.

- **Coma aberration**
  This is an aberration related to off-axis electrons. If some electron beams exit from a point on the object plane with a distance $r$ from the optical axis at various angles $\beta$ with respect to the optical axis, they do not come to a single point on the image plane, after the lens, but produce a cone-shaped (comet-shaped) image. The aberration effect is expressed by the relation: $d \sim C_{coma}r\beta^2$ and is, in general, corrected with beam tilt alignments.

- **Astigmatism**
  This defect can arise from a variety of contributions. It can occur when the electrons experience non-uniform magnetic field depending on the azimuthal angle, hence when the lens strength changes in transversal directions, loosing cylindrical symmetry. This aberration arises from the not perfect structure of the polepieces, that can present microstructural inhomogeneities which cause local variations in the magnetic field. Also the apertures, when not precisely centered around the axis or when is contaminated, can disturb the field and differently deflect the beam. The final results are always distortions in the images that can be quantified as proportional to the difference in focal lengths, $\Delta f$, induced by the astigmatism sources $d \sim \Delta f$. This aberration is easily corrected using stigmator (used both in illumination system and in imaging system), which are small octupoles that introduce a compensating field to balance the inhomogeneities.

- **Curvature of field** This aberration is correlated to the geometry of the lens system and deforms flat planes in curved planes. In this case, instead of a flat focal plane the microscope forms a curved focal surface; the focus, therefore varies with the radius from the optical axis and the consequent effect has radial symmetry. The created error is expressed as $d \sim r^2\alpha$. Curvature aberrations are corrected using smaller apertures and multi-lens systems.

- **Distortion** This aberration, differently from the others, created a distorted, and not a blurred images, modifying the shapes and the position of the features and not focus or resolution. It affect a microscope when the magnification changes with the distance from the optical axis and can be important in projector lenses. In general the distortion effect is proportional to the third power of the distance from the central axis ($d \sim r^3$). This aberration is corrected by calibration, software corrections or post-processing modifications.

### Chromatic Aberration

This aberration is related to the frequency (energy) of the electrons, that in the beam are not perfectly monochromatic. Depending on the electron source the energy spread may vary from $\sim 0.3$ eV to $\sim 1$ eV, but these values are small and generally do not affect image resolution. Chromatic aberration mainly occurs when the electrons interact with the specimen, emerge from it with energies spread over a certain range; once electrons reach the lens, they are bent in different ways by the magnetic field of the lens, producing a disk instead of a point in the image plane. Chromatic aberration gets worse with thicker samples. Energy filtering is the best solution to collect images or DPs with electrons that have lost substantial amounts of energy inside the specimen [2, 18].

### 1.3.3 Apertures

Apertures are often inserted into a lens and limit its collection angle. They are very important and allow to control resolution, contrast and many other characteristics of the image (or DP) formed by a lens. Apertures can also perform other functions, such as protecting the specimen from stray radiation in the illumination system, measuring the current in the beam or changing that current. Using apertures, it is possible to select certain electrons to pass through the lens and exclude others. Physically, the aperture may reside above, in, or below the plane of the lens. In general, they are circular holes in refractory metal disks (made of Platinum (Pt) or Molybdenum (Mo)), called diaphragms; these holes exist in several forms and thicknesses, depending on their function they can be individual disks with particular aperture or a series of different holes in single strip. Often the diaphragm collects and accumulate contaminations on the edge of the aperture caused by the electron beam cracking residual hydrocarbons in the vacuum. These accumulated materials destroy the aperture's circular shape and cause astigmatism or other problems, that can be overcome by cleaning or creating 'self-cleaning' diaphragms [2, 12].

### 1.3.4 Condenser System

Together with the electron gun, this constitutes the illumination system of TEM, in which electrons are taken from the source and transferred to the sample, defining all the properties of the beam (often called probe or spot) that illuminates the specimen. It consists of several lenses (in general called $C1, C2$ and so on) that work together. Two fundamental types of illuminations can be realized and they correspond to two basic different working mode of the microscope:

- **Parallel Illumination**
  The simplest way to realize this mode uses only two lenses: a first condenser lens $C1$ forms an image of the gun crossover and select the maximum current that illuminate the sample, and then, using a weakened and hence underfocused[1] $C2$, an underfocused image of the crossover

---

[1] **Focus, Underfocus and Overfocus**: A lens is said to be in focus when the image forms in the designated observation (image) plane, otherwise it is out of focus. A lens works in overfocus condition when its strength is increased such that

of the first condenser lens is produced, creating approximately parallel illumination in the image plane, in which the sample is placed. The $C2$ aperture here helps decreasing the angle of beam convergence and therefore make the beam more parallel (Fig. 1.5a). This first way to create parallel illumination can be improved using as a third lens the upper polepiece of the objective lens, which is always present in recent TEM columns, before the specimen. This is known as condenser-objective (c/o) lens ($C3$). In this new configuration, $C2$ takes the crossover of $C1$, but now it is focused at the front-focal plane of $C3$ and in this way a perfectly parallel illumination is created by this last lens on the sample (Fig. 1.5b). Hence, in parallel illumination the specimen is illuminated by an electron beam with a very small convergence angle, approximating a plane wave. This condition is essential in conventional image formation and in selected area DP.

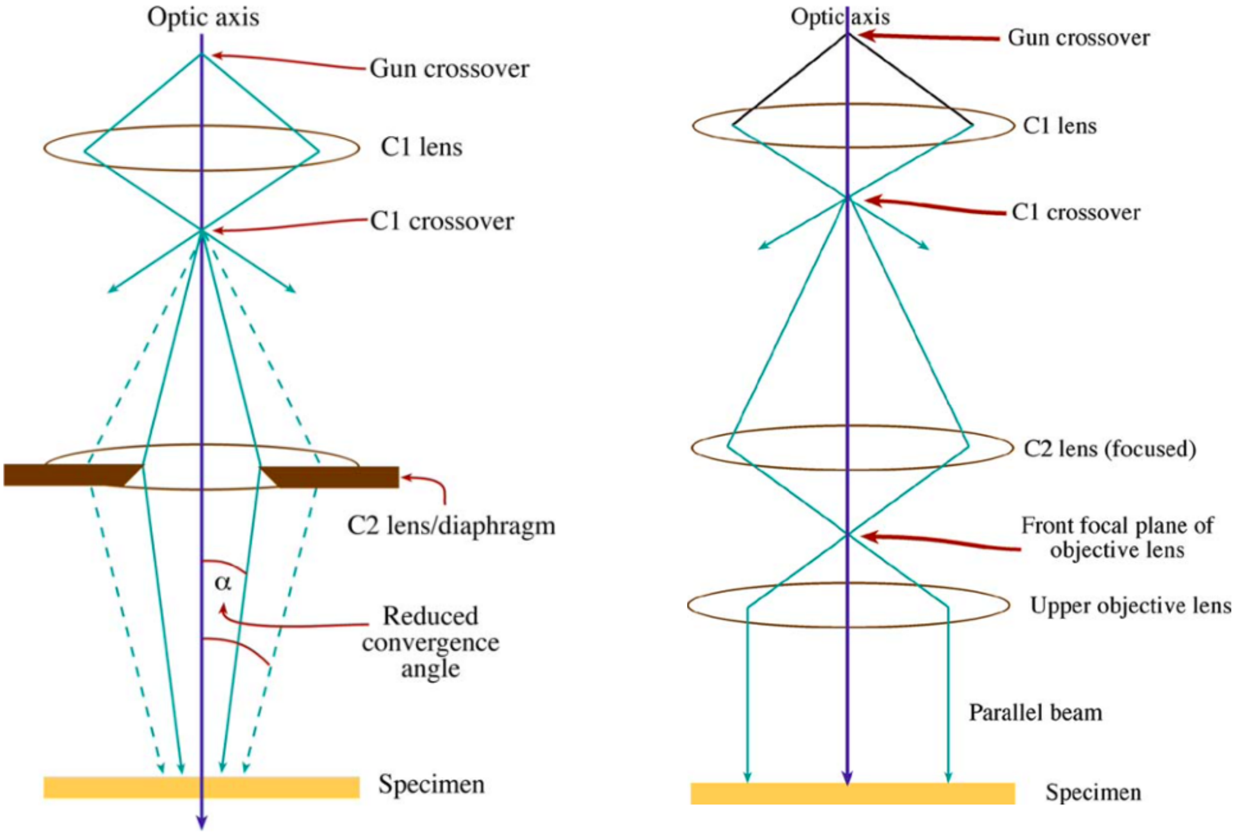

**(a)** **(b)**

**Figure 1.5:** Parallel beam illumination in TEM: (a) Using $C1$ and underfocused $C2$, with $C2$ aperture inserted in order to create a more parallel beam. (b) Using $C1$ and $C2$ to image the source at the front-focal plane of the c/o lens ($C3$).

- **Convergent Illumination**

  Using only two lenses, this condition is reached focusing $C2$ on the specimen, creating here

---

the image (crossover) forms above (before) the image plane. A lens works in underfocus condition when it is weakened and the image (crossover) forms below (after) the image plane [2] the image of the crossover of $C1$ (Fig 1.6a). In this way the beam is mostly convergent and, therefore, the intensity of illumination is very high, but the image contrast will be reduced and any selected area DP distorted because the sample is illuminated by many different incident angles simultaneously. The only possibility to see an image in this mode is to scan the beam over the specimen. The desired dimension of the probe to obtain reliable analyses is on the order of $\mathring{A}$ and can be obtained with just two lenses only using FEG. Again the usual solution is to introduce a third lens ($C3$, the upper polepiece of the objective lens), making it much stronger than usual and weakening (or switching off) $C2$ (Fig. 1.6b). To increase the demagnification action of $C3$ is also possible to strongly excite $C1$, increasing the object distance ($d_o$) for the c/o lens with respect to the image one ($d_i$) and hence obtaining a large demagnification (magnification: $M = -\frac{d_i}{d_o}$). Therefore $C1$ can be used to control the probe size at the specimen, but also the $C2$ aperture controls the convergence angle of the beam and is important to get the right converged spot size. With this illumination mode the intensity of the beam, is focused on a specific area of the sample and some specific techniques are possible.

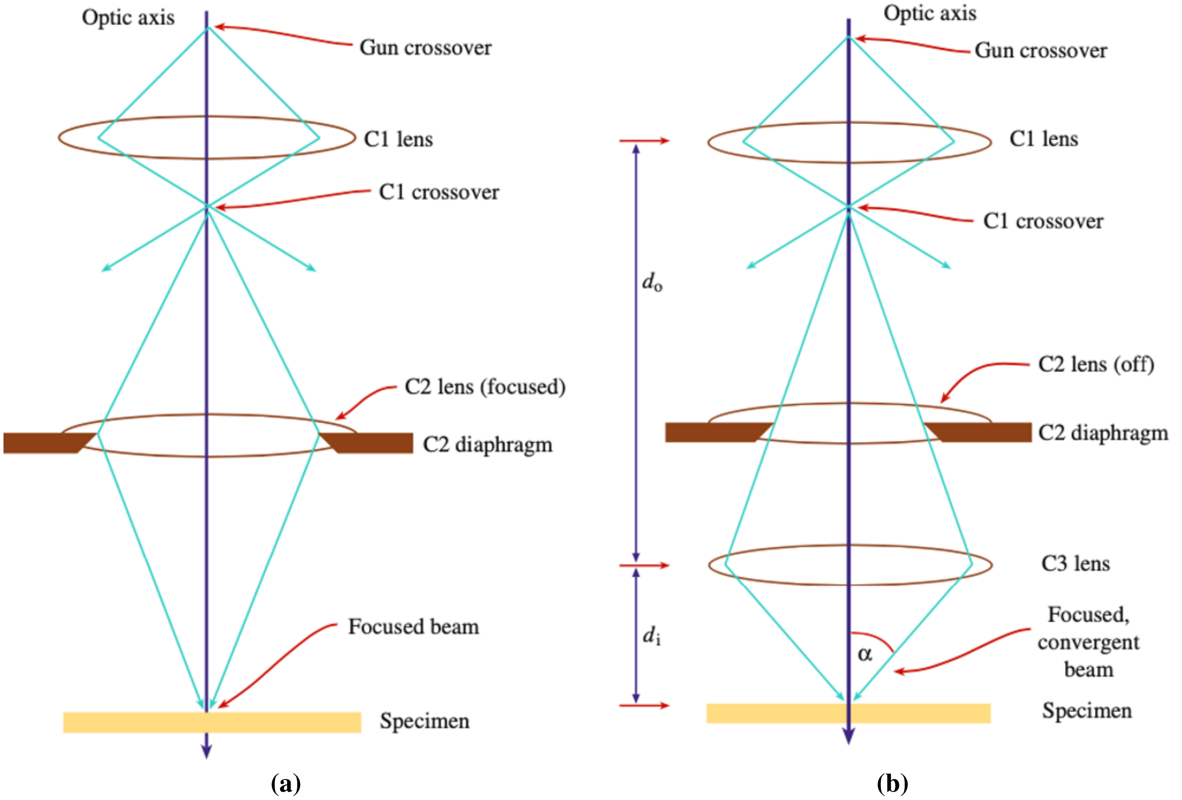

**Figure 1.6:** Parallel beam illumination in TEM: (a) Using $C1$ and $C2$, with an aperture in order to create a more parallel beam. (b) Using $C1$, $C2$ (switched off) and $C3$ to increase the convergence of the spot.

To be more accurate, the beam in c/o system is almost never perfectly parallel nor perfectly convergent, even using the condenser objective combination described before. For this reason, in TEM where both parallel and convergent beams are needed, another lens is generally introduced inside the illuminating system between $C2$ and the objective one. This lens is called condenser mini-lens ($C3$ or twin-lens) and operates in many different TEM modes, providing an additional degree of freedom. Changing the strength of $C2$ and the mini-lens excitations is possible to better control the illumination properties and the way in which the beam enters in the objective lens.

Scanning coils are another important part of the illumination system of TEM, useful when the beam needs to be laterally translated on the specimen or tilted off the optic axis to impinge the sample at a specific angle. Translating and tilting are essential for aligning the beam and are accomplished by varying the current through potentiometers, called scan coils, that create local magnetic fields that deflect the beam. Several sets of scan coils are present in the column and, using them, the beam in Scanning TEM (STEM) moves parallel to the optic axis illuminating step by step a different small area of the sample. This kind of scanning is realized by tilting the beam twice with two set of scan coils together with the already mentioned condenser and objective lenses (Fig 1.7). Scanning must not change incident beam direction as the beam is scanned, because if the incident direction varies the electron scattering processes would change when the beam intercepts the sample at different angles and the image becomes difficult (or impossible) to be interpreted [2, 12].

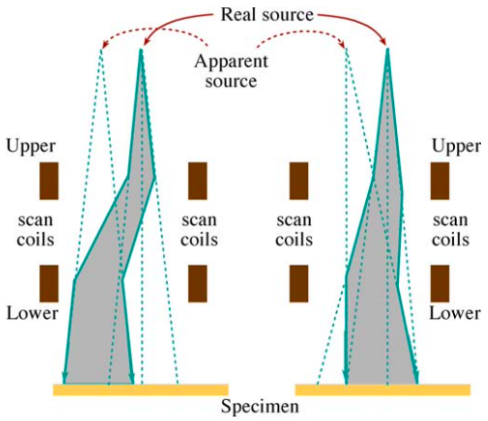

**Figure 1.7:** Scanning coils effects on the beam: On the left the translation of the beam, it remains parallel to the optic axis but illuminate a different area. On the right the tilting operation, in which the same area is illuminated form a different incident angle.

### 1.3.5 Objective Lens

The objective lens is the most important and strongest (2 T field) lens in TEM and exists in different versions. The most flexible objective lens is that in which the upper and lower polepieces are separated giving space to insert the sample and the objective aperture between these two parts. Thanks to its structure, it controls the illumination on the specimen (as already described, working together with condenser lenses) and takes the emerging electron from the exit surface forming the first intermediate image (or DP), which is then magnified and used by the following lenses. The electrons emerged from the sample can be dispersed by the objective lens to create a DP in the back-focal plane or can be recombined to form an image in the image plane. The quality of the objective lens determines the quality of the whole TEM system and of the information about the sample, because any error or aberration here is magnified and transmitted by all the other following lenses through the microscope. The split polepieces structure allows to excite differently the two parts of the lens: the upper one is generally very strongly excited, creating the right illumination on the sample, while the lower one focus the beam after the interaction with the specimen, like a conventional lens. This lens is always combined with the objective aperture, that can reside above, in or below the lens' plane and controls resolution, image contrast and many other properties of the collected data. It is the most difficult to construct lens, since the specimen must be located close to the center of this lens, limiting the defects but also the sample manipulation possibility [2, 12].

### 1.3.6 Imaging System

The imaging system uses several lenses to magnify (intermediate and diffraction lenses) the image or the DP created by the objective lens and to focus and project (projector lenses) these on the viewing screen or the detector. This part of the column can operate in two basic modes, that are described below and shown in Fig. 1.8. The imaging system presented here is highly simplified: most TEMs have many more imaging lenses which give greater flexibility in terms of magnification and focusing.

**Diffraction Mode**
To see DP the imaging-system lenses are adjusted so that the back-focal plane of the objective lens acts as the objective plane for the intermediate lens and then the pattern is projected on the image screen/detector. This mode is generally accomplished by means of a basic TEM operation in which only a specific area of the sample is selected to contribute to the DP; this selection (area reduction) can be realized in two different ways:

- **Convergent Beam Electron Diffraction (CBED)**
  Using $C2$ and $C3$ the beam is strongly converged on a specific small area of the sample, from which the DP is extracted. This operation destroys any parallelism and the spots are not sharply defined but spread into disks. In this technique the selection of the area happens before the specimen and only this one is illuminated.
- **Selected Area Electron Diffraction (SAED)**
  This is the standard way to perform diffraction mode by means of parallel illumination. In this technique, an aperture, called selected area aperture (SAD), is inserted in the image plane of the objective lens in order to select a specific area of the sample and to collect DP from it, excluding any electron that hits the specimen outside the defined area.

**Image Mode**
To look at an image the intermediate lens is set so that its objective plane is the image plane of the objective lens and again the resulting image is projected on the image screen/detector by the projector lenses. The two most basic imaging operations in TEM use the DP (so diffraction mode) to select specific spots by means of the objective aperture, placed in the objective lens back focal plane, and then, switching back to image mode, different images of the sample can be visualized.

- **Bright Field (BF) Imaging**
  Selecting the direct beam (central spot) in the DP a bright field image is created. In this way unscattered (transmitted) electrons are selected by the objective aperture and in the produced image the crystalline or high mass parts of the sample appear dark, while the parts in which the electrons are transmitted with less (or null) interactions appear brighter.
- **Dark Field (DF) Imaging**
  Selecting spots different from direct one in the DP a dark field image is visualized. In this way scattered electrons are selected by the aperture and hence the crystalline or high parts of the sample, in which the electrons have interacted, appear brighter in the image, while the regions with a lower number of scattering events appear dark.

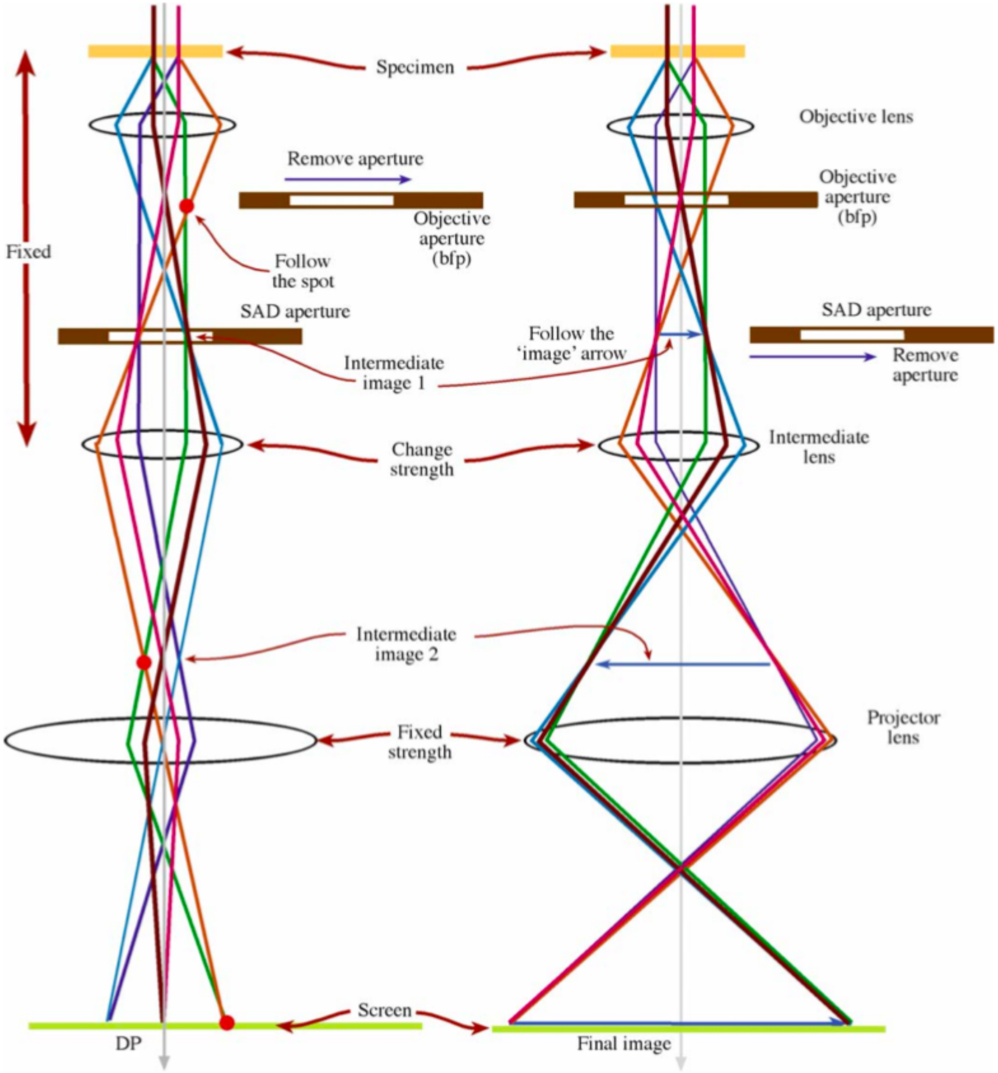

**Figure 1.8:** Two basic operations of the TEM imaging system. On the left the diffraction mode, with selected area diffraction aperture in the image plane; the intermediate lens uses as object the back-focal plane of the objective lens. On the right the image mode, with objective aperture in the back-focal plane; the intermediate lens uses as object the image plane of the objective lens. Then the projector lens projects the magnified DP or image on the screen. This is a highly simplified diagram with only three lenses.

Diffraction and imaging mode, as described here, are related to TEM, but similar modes can be realized also for STEM. In STEM the imaging system is simpler and no lenses (except for the objective one) are used to form the image, because the electrons are directly collected by detectors during the scanning to form the final image. Dark field and bright field in STEM are performed using different detectors, placed in distinct positions in order to collect differently scattered electrons, selecting them through their scattering angles [2, 12].

### 1.3.7 Detectors

Images and DPs, that are produced by the imaging system, are different distributions of electron intensity (or density) and they need to be visualized. There are different ways to 'see' electrons and the digitalization of the detected image has a crucial role in all the subsequent analysis that can be performed on the experimental data. Electrons are detected and displayed in different ways depending on whether TEM or STEM are used. The basic phenomenon used to visualize electrons is cathodoluminescence (CL), in which the energy of the electrons is used to produce light and therefore the screen will emit light in proportion to the intensity of electrons falling on it. The most important detectors are presented below:

- **Viewing Screen**
  These are fluorescent screens covered with materials such as zinc sulfide (ZnS) small grains, generally doped, that emit visible light (typically green) when hit by electrons. This traditional analog detection allowed the operator to directly visualize the image or the DP, but in modern TEM this approach has been replaced by digital detection systems, which enable image acquisition, storage and analysis.
- **Semiconductor Detectors**
  They are doped single-crystal sheets of silicon (Si), with a p-n junction beneath their surface, which makes them electron-sensitive. The junction can be created in Si by means of doping through ion implantation or by means of evaporation of gold (Au) on its surface if Si is n-type or of aluminum (Al) when it is p-type (surface-barrier detector). When these detectors are placed into a beam of high-energy electrons, the energy is transferred to valence band electrons of Si that are excited across the gap, creating electron-hole pairs, which can be separated by applying a reverse external bias to the detector (or are in practice separated by the internal p-n junction bias). The result is that the incoming electron signal is converted into a current in the external circuit, between the surface junction contacts. These detectors are very efficient in collect and amplify electron signals, are cheap, easily fabricable and can be cut in any shape, but they are not very responsive to rapid changes in signal intensity, present noise, have slower response and are insensitive to low-energy electrons. An example of this device is presented in Fig. 1.9a.
- **Scintillator-Photomultiplier (PM) Detectors/TV Cameras**

Scintillators emit visible light when struck by electrons and are made of materials such as $Ce$-doped Yttrium-Aluminum Garnet (YAG) and various doped plastics and glasses that have decay times of ns, in order to be sensitive to rapid changes of intensity. The visible light is then amplified by a photomultiplier system. In general the scintillator surface is coated with a layer of reflecting material (Al) that stops the light generated in the microscope from entering in the detector. Their noise is smaller than the one in semiconductor devices and they are more sensitive to signal changes. This detector however is less robust, less manufacturable and more expensive than semiconductor one. The TEM image can be viewed directly through a TV camera, rather than looking at the fluorescent screen and this leads to several advantages. Cameras are in general placed below the viewing screen. An application of this detector to secondary electrons in presented in Fig 1.9b.

- **Charge-Coupled Device (CCD) Detectors** They are metal-insulator-silicon devices that store charge generated by light or electron beams. CCD consists of arrays made of several (millions of) pixels, which are individual capacitors electrically isolated from each other through potential wells under each CCD cell (Fig. 1.9c). Each pixel accumulates charge in proportion to the incident radiation intensity. To create an image the array needs to be read out by changing the applied potentials to transfer the charge serially from each potential well along a line in the array into an output amplifier. Once all the cells are empty the array can be re-exposed, this full-frame design is simple and robust. When shorter frame times (and so faster image acquisitions) are needed the whole frame can be transferred to an adjacent storage array, leaving the main array free to collect new signal flux. Reading times depend on the size of the image and on the used technology to read out the array. When cooled they have very low noise and good sensitivity, they present also a very good and uniform response across many pixels. This system is expensive and drawbacks can occur: one example is blooming, when a pixel collect too much signals and they overflow into surrounding pixels. They are used for real time TV recording.

In TEM different electrons can be detected (unscattered, forward scattered, back-scattered and secondary). Semiconductor detectors are only sensitive to electron with sufficient energy (> 5 keV), so they are used to detect high-energy forward-scattered and high energy back scattered electron images (not too performed in TEM). For low energy secondary electrons is generally used a more sensitive scintillator system and in some cases electrons are accelerated in order to penetrate inside the detectors. In STEM, in which a quick response is needed, TV images are the normal viewing mode and scintillator-PM system is preferred to semiconductor detectors, thanks to its rapid signal response and high sensitivity. As already mentioned, in STEM several detectors are positioned to collect electrons at different angles. The bright-field (BF) detector is located on the optical axis and collects forward-scattered electrons at very small angles ($\alpha < 10$ mrad). Annular dark-field (ADF) detectors collect electrons scattered to intermediate angles ($10 < \alpha < 50$ mrad) using a ring-shaped detector. At even larger scattering angles ($50 < \alpha < 200$ mrad), high-angle annular dark-field (HAADF) detectors collect incoherently scattered electrons [2, 12].

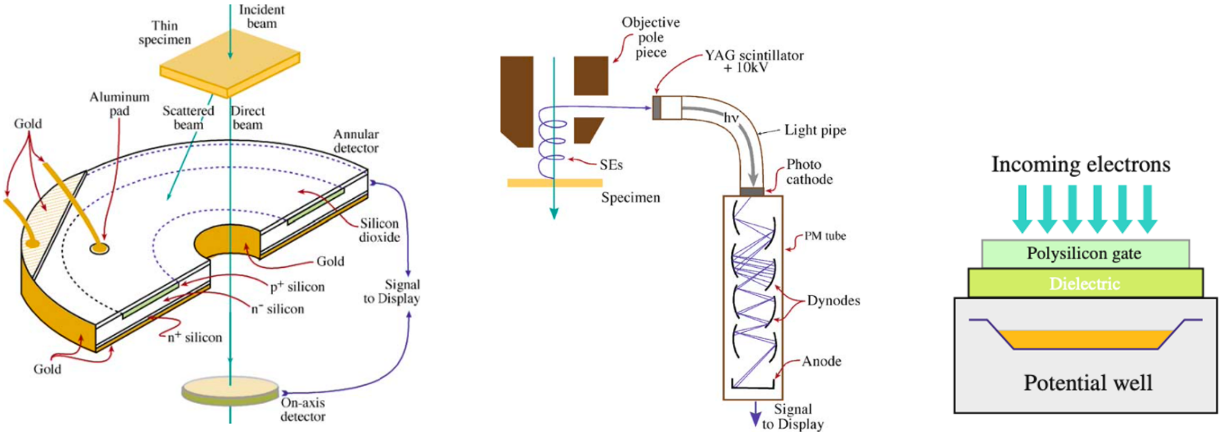

**(a)** **(b)** **(c)**

**Figure 1.9:** Electron Detectors: (a) Semiconductor device: surface-barrier type with the p-n junction created in doped Si and with Au wire connections. An on-axis detector detects the forward-scattered electrons, while the anular one collects the scattered electrons. (b) Scintillator-Photomultiplier: in this sketch applied to secondary electrons, that are accelerated onto the YAG scintillator, generating visible light, that travels, is reconverted to electron signal and is amplified (by several electrodes) and redirected to the display screen. (c) Single CCD-cell: it storages the charge in a potential well under one pixel.

### 1.3.8 Pumps and Holders

Other two important parts in TEM column to mention are the vacuum system and the sample holder.

Electrons must travel under vacuum to avoid scattering with other atoms in the environment inside the column. Vacuum helps also in keeping the specimen clean and avoids and limits contaminations from hydrocarbons and water vapor introduced by the holder. Vacuum in the stage of typical TEM is $10^{-5}$ Pa, which is in the high vacuum range, and this value is typically kept permanently fixed. All the accesses to change specimens or to carry out other operations are performed via an airlock system, which can be pumped separately. In general a type of vacuum pump is used to create a rough vacuum and another type, working in series, is used to create higher vacuum. In modern TEM at least two separate pumping systems are present: one for the column and one for the camera and screen chamber. If the source is a FEG a separate ultra high vacuum pumping system is added in the gun region. In most TEMs the stage and gun have significantly better vacuums than the camera region. Different vacuum chambers communicate through specific valves and differential pumping apertures and generally the vacuum system is fully automated.

The holder is the removable device that allows to insert the specimen inside the column and its quality can affect the quality of the data generated by the microscope. The specimen holder assembly is inserted into the TEM stage, the mechanical system of the microscope that controls movements and position of the holder. Historically, two designs exist: the side-entry holder, a rot with motor attached to tilt and/or rotate the specimen that remains mechanically in contact connected to the outside, and the top-entry holder, a cartridge that is load from the top of the column into TEM stage mechanism and remains detached from the outside world during the microscopy session. In general the specimen is inserted in the holder inside a small cup (2 ÷ 3 mm). Side-entry holders are more versatile, can hold larger samples and are today the standard. However connection with the outside environment, via a long lever arm, can more easily transfer vibrations, cause thermal drift or create vacuum disturbance during the insertion. There exists holders with a lot of different properties, based on their capability to tilt, rotate, hold more than one sample, heat, cool and admit specific analyses or measurements [2, 12].

### 1.3.9 Ray diagrams and quantitative aspects of TEM

All of the parts presented in the previous sections together form the TEM column. The exact configuration of the column depends on the specific microscope and on the measurement technique adopted, but the fundamental layout is generally similar and the basic ray diagrams are presented in the following images for TEM and STEM in image mode (Fig. 1.10). Similar diagrams can be created for any kind of TEM mode and technique. As already mentioned, these ray sketches are simplified and can be realized because of the behavior of electron beams in magnetic lenses can be described using concepts analogous to those of geometrical optics.

These diagrams reconstruct, step by step what happens inside TEM column during the measurement. The electron beam is generated by the source at an accelerating voltage generally between 80 and 300 kV, the gun crossover is then demagnified by two or three order fo magnitude and focused onto the sample by the condenser lenses. Condenser system controls the illumination conditions, allowing parallel illumination with an aperture of 0.01 ÷ 1 mrad and convergent illumination, producing a focused probe with 0.2 ÷ 100 nm diameter. The objective pre-field contributes to the probe formation on the sample and its post-field collects the transmitted electrons, forming the first magnified image (20 ÷ 50 times). The image is finally magnified and projected by the imaging system that can reach total magnifications in the range $10^2 \div 10^7$ times. Diaphragms with different diameters ($10 \div 10^3$ $\mu$m), together with aberrations correctors control and shape the beam across the whole column until it reaches the detector, producing final images and DP with spatial resolutions that can approach 0.1 nm or lower values in modern instruments [2, 12].

## 1.4 What can be observed with TEM

To obtain any information using transmitted electrons, the specimen has to be 'thin' enough to transmit sufficient electrons to reach and be detected by the detector. 'Thin' is a relative term and is strictly related to electron energy and to the atomic number ($Z$) of the involved material. Increasing the accelerating voltage and so the electron energy, their penetration depth increases,

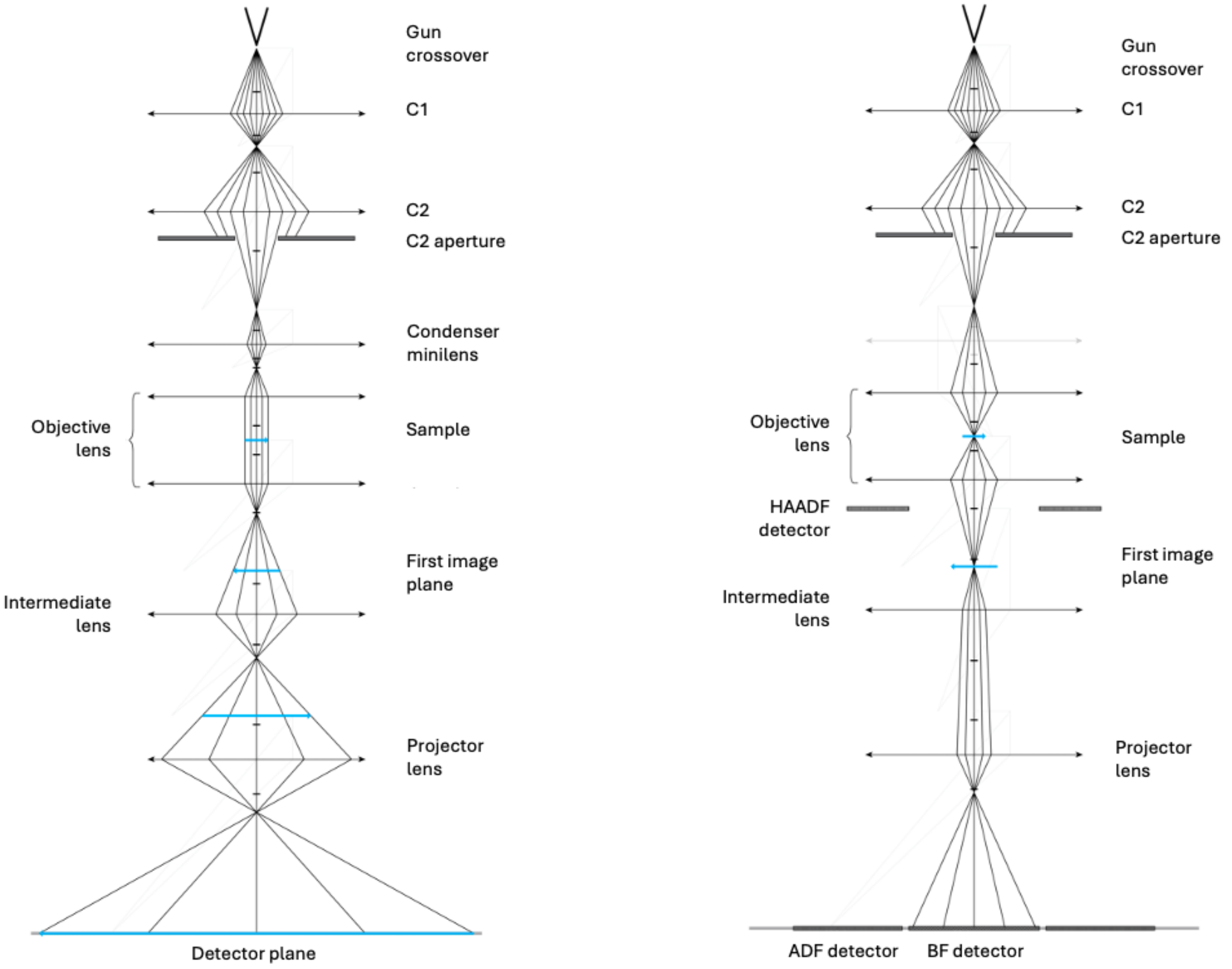

(a) (b)

**Figure 1.10:** Ray diagrams: (a) TEM. (b) STEM. They presents the fundamental elements and result from the combination of all the elements presented in previous sections. Images adapted from EPFL website [19].

allowing thicker sample to be investigated, while materials with higher $Z$ scatter electrons more strongly and therefore require thinner specimens. In practice, specimens with thickness lower than 100 nm are used wherever possible and thinner regions are often required for high-resolution imaging. While increasing the beam energy relaxes thickness constraints, it may also enhance beam-induced damages on the sample (for example local heating, radiolysis, atomic displacements and charging). For this reason, beam-sensitive materials are in general avoided or treated with specific precautions, such as low-dose imaging, cryogenic techniques and other techniques. The studied materials have also to be chemical stable and resistant to contaminations. Under these conditions, a wide variety of materials can be studied using TEM: crystalline materials, such as metals, alloys, ceramics, semiconductors and minerals, nanostructured materials, such as nanoparticles, nanotubes, nanowires and thin films, but also soft and biological materials. In general, appropriate preparation techniques are typically required to produce samples with the properties described above [2, 20].

From the described samples, several types of information and properties can be extracted using TEM. Materials can be characterized from structural (crystallographic), morphological and chemical point of view. Imaging modes like BF and DF allow the investigation of microstructures, interfaces and defects, while High-Resolution TEM (HRTEM) enables the direct observation of lattice fringes and atomic arrangements, pushing the microscope to its maximum optical resolution. Crystallographic information can be obtained through electron diffraction techniques (SAED and CBED), providing crystal structures, defects and orientations. Chemical composition and electronic structure are analyzed by spectroscopic techniques based on the energy of the detected electrons, such as EELS and Energy-Dispersive X-ray Spectroscopy (EDS). Similarly, in STEM these properties can be extracted, by rastering the probe across the sample, point by point, acquiring structural and spectroscopic signals. Furthermore, using electrons, electromagnetic properties are accessible, always with a nanometer resolution. For this reason, electrostatic potentials, magnetic structures and fields and other electromagnetic information can be extracted from the phase of the electron wave by means of advanced techniques and reconstructions methods (for example electron holography, Lorentz TEM and differential phase contrast) [2, 12].

# Chapter 2

# Wave-optical description of electrons and phase shift formation

Electrons can be described as particles, as seen in the previous chapter, but it is not possible to make any meaningful TEM investigation without considering electrons in their wave nature. This chapter presents the wave behavior of the electron and introduces the theoretical framework to describe the interaction between an electron beam and a specimen in transmission electron microscopy, with particular emphasis on phase-related phenomena. In the wave-optical description the electron beam is now treated as a coherent wave with amplitude and phase that evolve during the propagation through the microscope column and the interaction with the sample. Phase and amplitude therefore contain all the information about the specimen, but through conventional detection methods the phase part is completely lost, creating the well-known ’phase problem in electron microscopy’. In particular, the interaction between electrons and electromagnetic field related to the specimen is discussed in a quantum mechanical approach, leading to the derivation of the phase shift acquired by the electron wave. The phase modulation depends on electrostatic and magnetic potentials and particular attention is devoted to the magnetic contribution. Furthermore, the physical meaning of the magnetic phase shift is deepened through the Aharonov-Bohm effect, focusing on the crucial role of the magnetic vector potential and on the relation between phase and enclosed magnetic flux. Finally, the model of a uniformly magnetized sphere is introduced and its magnetic phase shift is derived and simulated. This serves as the starting point for the development of more complex simulations and provides a reference framework for the interpretation of experimental results and for the analysis of magnetic nanostructures investigated in this work.

## 2.1 Electron wave description in TEM

Electrons are quantum particles governed by quantum mechanics laws and, in this framework, are described by a complex wavefunction; their space-time behavior cannot be perfectly predicted and only probabilities for finding electrons in a region of space can be determined. The particle model of the fast electron, presented in Section 1.3.2, is a useful approximation to describe specific situations such as the behavior in a magnetic lens and the fundamental scattering events. However, a complete description of electron propagation and image formation in TEM requires a quantum mechanical based wave-optical model. Depending on the experiment, electrons are considered as particles or as waves, hence both models are important, but mostly in TEM and always in HRTEM and holography they appear in their wave-nature, because interference and phase modulation effects become fundamental. Within this description, the electron beam is represented by a complex wave function in which amplitude and phase must be considered. The general wavefunction expression for electron is:

$$\psi(\mathrm{r}) = a(\mathrm{r})e^{i\varphi(\mathrm{r})} \tag{2.1}$$

where $a(\mathrm{r})$ represents the amplitude of the electron wave and $\varphi(\mathrm{r})$ its phase, both depend on the position vector $\mathrm{r} = (x, y, z)$. The phase term contains the information related to the interaction of the electron with electromagnetic field in the specimen and will be fundamental in this work. The intensity associated with this wave is given by:

$$I(\mathrm{r}) = |\psi(\mathrm{r})|^2 = |a(\mathrm{r})|^2 \tag{2.2}$$

Equation (2.2) reveals that phase information is lost when the electron intensity is recorded. This ”phase problem” constitutes one of the main motivations of this work and it will be examined in greater depth in the following sections from a theoretical and an experimental point of view. In this wave-optical treatment, the electron beam is considered quasi-monochromatic, with a well defined energy determined by the accelerating voltage. Under these stationary conditions, the wave function can be separated into spatial and temporal components, where the time dependence reduces to a global phase factor, which is uniform and has no observable consequences. As a result, the whole problem can be treated using time-independent formalism, omitting the time.

Electrons emitted from the source can therefore be regarded as coherent waves that propagate along the microscope column, according to the laws of wave optics. The electron wave is focused and deflected by the electron-optics described in the first chapter and can be generally approximated as a plane wave when it illuminates and interacts with the sample. This interaction modifies (modulates) both the amplitude and the phase, creating the so-called object wave. This object wave carries information about the specimen, encoded in its amplitude and phase and it is transferred by the imaging system to the detector plane, where the intensity distribution is measured, creating the final image. The recorded image contains the intensity (expressed in Eq. 2.2), and therefore it cannot provide direct access to the phase information, but only to the amplitude one. The described image formation process is reported in Fig. 2.1.

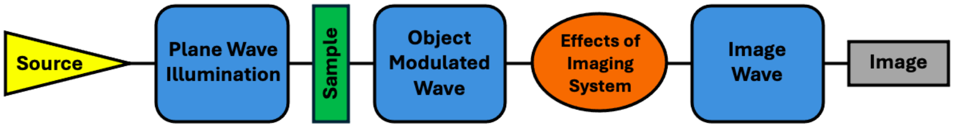

**Figure 2.1:** Image formation in TEM: Schematic representation in wave optic approach. Sample is illuminated by a plane wave, that interact with it creating a modulate object wave. Then the wave is modified also by the imaging system creating the image wave, that is detected and represented, through its intensity, in the image.

TEM images are thus determined by how the information encoded in the electron wave is transferred during its propagation through the microscope. For this reason, a wave-optical description of electron propagation in the microscope is essential to interpret and understand image formations and phase-sensitive techniques, such as electron holography[21, 22].

## 2.2 Phase problem in electron microscopy

As presented in Section 1.3.7, electron detectors record a signal proportional to the intensity of the electron wave. Therefore, a conventional TEM image represents the square modulus of the electron image wavefunction (as described in the previous section and shown in Eq. 2.2), while the phase contribution is not directly recorded and is lost. The absence of direct phase information leads to the loss of fundamental properties about the specimen, since, as will be discussed, many physical characteristics are primarily encoded in the phase of the transmitted wave. This fundamental limitation is known as the phase problem in electron microscopy.

In order to fully understand the significance of the phase problem and the importance of its resolution, it is essential to present what physical information is encoded in the phase of the electron wave. This requires a quantum-mechanical description, which allows for a rigorous treatment of the wave function and its interaction with the specimen [23, 24]

## 2.3 Phase shift induced by electrostatic and magnetic fields

The interaction of the electron wave with the sample results in both amplitude and phase modulation. Amplitude variations are directly observable in the recorded intensity (amplitude contrast) and arise from scattering, absorption processes and mass-thickness effects. On the other hand, phase modulations are generated by electrostatic and magnetic potentials inside the specimen and in particular, the magnetic contribution affects only the phase of the electron wave. In general, the imaging system converts phase variations into intensity variations and, as a result, phase can indirectly affect the intensity in the final image, for example in the form of lattice fringes at high resolutions and Fresnel fringes at interfaces (phase contrast) [2].

The phase modulation is associated with the interaction of electrons with electromagnetic fields inside the material. When the electrons cross the sample, they accumulate an additional phase shift, that depends on the potentials encountered along their trajectory. This behavior can be rigorously described within the framework of quantum mechanics, obtaining an expression for the total phase shift as the combination of electrostatic and magnetic contributions.

Starting from a time-independent spin-free Schrödinger equation for an electron wavefunction in the presence of an electric and a magnetic field, expressed in terms of their potentials:

$$\frac{1}{2m}[-i\hbar\boldsymbol{\nabla} + e\mathrm{A}(\mathrm{r})]^2\psi(\mathrm{r}) - eV(\mathrm{r})\psi(\mathrm{r}) = E\psi(\mathrm{r}) \tag{2.3}$$

where $\boldsymbol{A}(\mathrm{r})$, $V(\mathrm{r})$ and $\hbar$ are the magnetic vector potential, the electric potential and the reduced Planck constant, respectively. $E$ is the total electron energy. For the high-energy electrons used in TEM, relativistic effects are significant and are taken into account through corrections to the electron mass, wavelength, and energy in the subsequent treatment. By expressing the electron wavefunction in the form of Eq. 2.1 and applying the paraxial approximation, this equation can be simplified and split into two coupled equations:

$$[\hbar\nabla\varphi(\mathrm{r}) + e\mathrm{A}(\mathrm{r})]^2 = 2m(E + eV(\mathrm{r})) + \hbar^2\frac{\nabla^2 a(\mathrm{r})}{a(\mathrm{r})} \tag{2.4}$$

and

$$\nabla \cdot [a(\mathrm{r})^2(\hbar\nabla\varphi(\mathrm{r}) + e\mathrm{A}(\mathrm{r}))] = 0 \tag{2.5}$$

These two equations, working within eikonal and phase object approximations, can be simplified and the electron propagation can be described analogously to light in geometrical optics. In this framework, an effective refractive index for electrons is introduced and used to evaluate the optical path of the electrons between two points. Finally, considering $U^* \gg eV$, the phase shift of the electron wave, after the interactions with the electric and magnetic fields, is extracted as the the optical path difference between an electron in a region with electromagnetic field and one in an unperturbed (vacuum) area. The resulting phase shift, in cartesian coordinates, presents two important contributions:

$$\varphi(x, y) = \varphi_{el} + \varphi_{mag} = C_E \int_{-\infty}^{+\infty} V(x, y, z)\, dz - \frac{\pi}{\phi_0}\int_{-\infty}^{+\infty} A_z(x, y, z)\, dz \tag{2.6}$$

where $C_E = \frac{2\pi}{\lambda}\frac{E+E_0}{E(E+2E_0)}$ is the relativistic corrected interaction constant (with $\lambda$ the wavelength, $E_0$, the rest mass energy of the electron and $E = eV_{acc}$ the electron energy due to the accelerating voltage $V_{acc}$), $\phi_0 = \frac{h}{2e}$ is the flux quantum and $A_z$ is the component of the magnetic vector potential parallel to the electron beam direction [23, 25].

The first term of the phase shift represents the electrostatic contribution. It is energy dependent, through the constant $C_E$ (determined by the accelerating potential of the microscope), and involves the integral of the electrostatic potential $V$ along the beam direction (also called projected potential). If no external charge distributions or applied electric field are present within or around the specimen, this contribution is dominated by the internal potential of the sample. For a homogeneous material, the electrostatic potential can be approximated by the mean inner potential $V_{MIP}$, defined as the spatial average of the electrostatic potential within the unit cell. This quantity represents the average potential arising from the superposition of atomic potentials in the material ($V_{MIP} =$

$\frac{1}{Vol}\int_{Vol} V_{atom}\, dxdydz$). Under these approximations the electrostatic contribution reduces to:

$$\varphi_{el} = C_E V_{MIP} \int dz = C_E V_{MIP} t(x, y) \tag{2.7}$$

where $t(x, y)$ is the local thickness of the sample. This linear expression provides a simple and widely used relation connecting the electric phase shift to the specimen thickness an its average potential.

The second term in Eq. 2.6 represents the magnetic contribution to the phase shift and carries information about the magnetic induction vector within the sample. This part is independent of the electron energy and depends only on the spatial distribution of the magnetic vector potential. It is directly related to the magnetic flux enclosed by the electron trajectory and is important for the magnetic characterization of materials. The magnetic phase shift is fundamental in this work and will be better described in Section 2.4.

Eq. 2.6 thus fully expresses how the phase of the electron wave is modified by its interaction with the sample and describes the phase modulation that the wave acquires. The sample is considered as a collection of electrostatic and magnetic potentials that interact with and change the phase of the electron wave (Fig. 2.2). Although the phase is not directly accessible in conventional imaging, it can be retrieved using, for example, interference-based techniques (presented in Chapter 3, providing important physical information about the studied material [26].

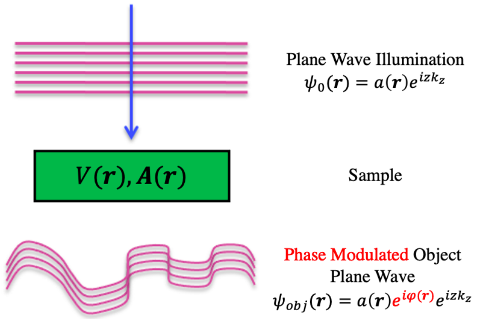

**Figure 2.2:** Phase modulation after interaction with the sample: Schematic representation. Plane wave is modulated interacting with the potentials inside the specimen and this a phase shift in the electron wave.

## 2.4 Magnetic phase shift and Aharonov-Bohm effect

The magnetic contribution to the electron phase shift arises from the interaction with the magnetic vector potential A.

$$\varphi_{mag} = -\frac{\pi}{\phi_0} \int_{-\infty}^{+\infty} A_z(x, y, z)\, dz \tag{2.8}$$

This phase term depends on A rather than directly on the magnetic field B. As a consequence, a magnetic phase shift does not require that electrons experience a Lorentz force ($\mathrm{F_L} = e\mathrm{v} \times \mathrm{B}$) and can arise even in regions where $\mathrm{B} = 0$. This is the Aharonov-Bohm effect and was firstly predicted in 1949 by Ehrenberg and Siday [27]. Ten years later, Aharonov and Bohm reformulated this phenomenon in quantum mechanics, stating, contrary to classical mechanics, that there exists effects of potentials on charged particles even in the region where all the fields (and therefore the forces) vanish [28]. This effect was experimentally verified by R. Chambers one year later, in 1969 [29], and then by electron holography experiments [25, 30].

Potentials were once regarded as a mathematical convenience and interpreted as having no real physical significance. In quantum mechanics, interaction between electrons and an electromagnetic field is specified by potentials and the true question was whether they are a fact or not in this context. The Aharonov-Bohm effect demonstrates that an electron beam is physically influenced while passing through a space in which there are no fields but only potentials. A typical configuration for this effect is illustrated in Fig 2.3, in which a magnetic field is produced only inside a infinite solenoid, by applying an electric current to it, while outside B = 0. Two coherent electron beams, produced from a point source, pass on both sides of the solenoid, and are overlapped to form an interference pattern and to measure the phase difference. Despite the absence of B along the electron trajectories, a phase difference proportional to the flux inside the solenoid is measured in the pattern. This demonstrates that the electron phase is sensitive to the magnetic vector potential. Outside the field and therefore the curl of A is zero ($B = \nabla \times A$), but this does not imply that also A is null. This seems not possible from classical point of view, but it is a direct consequence of the Schrödinger equation [30].

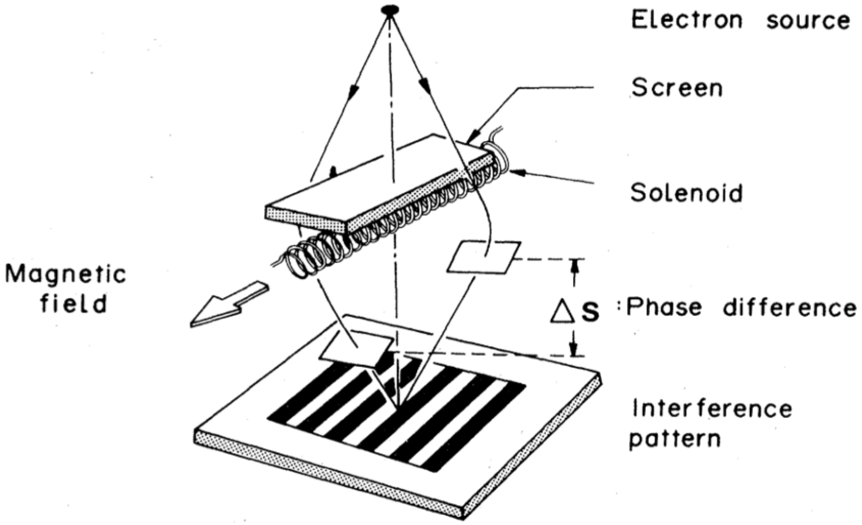

**Figure 2.3:** Aharonov-Bohm effect: typical configuration. Two electron beams pass on both sides of an infinite solenoid. Their phase difference is evaluated from an interference pattern and is measured as proportional to the magnetic flux produced between the two beams.

This concept can be deepened by demonstrating that the magnetic contribution to the phase shift carries information about the magnetic flux. In order to formalize this, the phase difference between two arbitrary points in a magnetic phase image, at coordinates $(x_1, y_1)$ and $(x_2, y_2)$, is computed, using Eq. 2.8:

$$\Delta\varphi_{mag} = \varphi_{mag}(x_1, y_1) - \varphi_{mag}(x_2, y_2) = -\frac{\pi}{\phi_0}\int_{-\infty}^{+\infty} A_z(x_1, y_1, z)\, dz + \frac{\pi}{\phi_0}\int_{-\infty}^{+\infty} A_z(x_2, y_2, z)\, dz \tag{2.9}$$

The last sum of integrals can be recast as loop integral, considering a rectangular loop formed by the two parallel electron trajectories, crossing the sample at the two point coordinates and closed by perpendicular paths at infinity. Then, through the relation between A and B, the Stoke's theorem can be applied, leading to:

$$\Delta\varphi_{mag} = \frac{\pi}{\phi_0}\oint \mathrm{A}\cdot \mathrm{dl} = \frac{\pi}{\phi_0}\iint \mathrm{B}\cdot \mathrm{dS} = \frac{\pi}{\phi_0}\Phi_{mag} \tag{2.10}$$

where $\Phi_{mag}$ is the magnetic flux enclosed in the loop described by the two considered electron beam trajectories and it depends on the two chosen points in the magnetic phase image [21, 26].

This result highlights that the magnetic phase shift is directly related to the enclosed magnetic flux and not to the local value of the magnetic field. Even in the presence of a non-zero B-field in which the electrons experience the Lorentz force, the phase shift remains determined by the total flux enclosed by the electron trajectories. For this reason, a difference in the magnetic phase inside of an image is a clear fingerprint of the presence of a magnetic flux in the analyzed region. Eq. 2.8 and 2.10 summarize the quantum mechanical origin of the magnetic phase shift and its relations with the fundamental magnetic properties of materials, that can be extracted from $\varphi_{mag}$ to characterize them [23].

## 2.5 Magnetic phase shift simulations

The relation between the phase shift and the enclosed magnetic flux provides the theoretical basis for quantitative magnetic imaging in TEM. In order to interpret experimental results in practical applications, it is often useful to model the expected phase shift for specific magnetic configurations. The comparison between simulated and experimental phase images represents an important tool for the analysis and characterization of the investigated systems. Through simulations, a qualitative and quantitative understanding of the expected phase distribution is possible and this helps in evaluating the accuracy and reliability of the experimental data. In this section, a simple model is introduced, the corresponding phase shift is computed and then the phase of more complex systems are simulated, by arranging together some simple components.

### 2.5.1 Uniformly magnetized sphere phase shift

Starting from Eq. 2.8 and from the knowledge of the magnetic vector potential A(r), analytical expressions for the phase shift can be derived for specific magnetic configurations. As a fundamental reference case, the uniformly magnetized sphere of radius $R$ and magnetic moment $\mu$ is considered. This model represents the simplest system that captures the essential features of magnetic phase contrast and serves as a starting point for the description of more complex nanostructures. From the work of de Graef et al. in 1999 [31], this magnetic phase shift can be expressed as:

$$\varphi_{mag}(x,y) = \frac{\mu_0 \mu}{2\phi_0} \frac{x}{x^2+y^2} \begin{cases} 1-(1-\frac{x^2+y^2}{R^2})^{\frac{3}{2}} & x^2+y^2<R^2 \\ 1 & x^2+y^2>R^2 \end{cases} \tag{2.11}$$

where $\mu_0$ is the permeability of vacuum ($\mu_0 = 4\pi \times 10^{-7}$ H/m) and the magnetization ($M = \frac{\mu}{V}$) is oriented along the $y$-axis. In this framework, the electrons travel along the $z$-axis and the sphere is placed on the $(x,y)$-plane. The corresponding magnetic phase map is shown in Fig. 2.4.

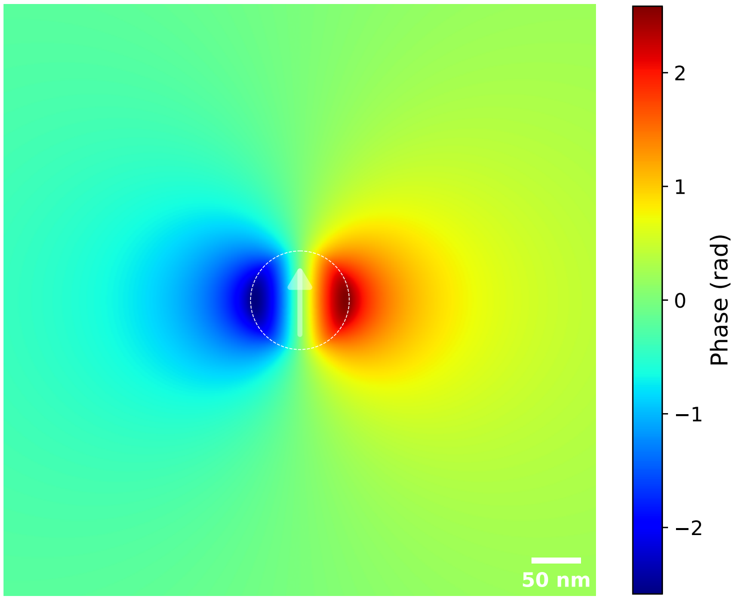

**Figure 2.4:** Uniformly magnetized sphere - magnetic phase simulation: Phase map simulated for a 50 nm radius sphere, magnetized with magnetization $M \simeq 7.95 \times 10^5$ A/m along y-axis. Field of view (FoV) of 0.6 $\mu$m. The white arrow points out the magnetization direction, while the white dashed line highlights the original dimension of the sphere.

This map presents the typical magnetic phase behavior with two lobes of opposite sign, symmetric with respect to the magnetization axis and with a strong phase gradient at the center, where $\varphi_{mag}(x,y) = 0$. The two-lobes structure originates from the dipolar nature of the uniformly magnetized sphere, with field lines that exit from one side of the dipole and enter on the other, while the magnetic vector potential circulates around the magnetization axis. The electrons, crossing the sample, experience opposite projected contributions of the vector potential on the two sides of magnetization axis; this results in opposite phase shift sign and creates this dipolar distribution. The magnetization in this simulation is set to $M \simeq 7.95 \times 10^5$ A/m, corresponding to a characteristic magnetic field associated with the magnetization $B_0$ of 1 T in absence of external field (hence with $B_0 = \mu_0 M = 1$ T). This value is representative of ideal and typical saturation magnetization for metallic magnetic nanoparticles based on iron (Fe) or cobalt (Co) [32, 33]. This kind of magnetization produces around 2 rad with phase variations inside and around the sphere on the order of the fractions of radians.

To emphasize the characteristic behavior of this phase object, in the following image (Fig. 2.5), the cosine of the amplified phase ($\cos(10\ \varphi_{mag})$) is plotted, together with a line profile traced through the center of the sphere and perpendicular to its magnetization axis. Plotting the cosine of the phase enhances the visibility of the spatial gradients and phase differences, by means of the analytical non linear response of cosine function. Furthermore, multiplying the phase by an amplification factor (10 in this example) improves the visualization of small phase variations, which would otherwise produce weak contrast. This operation is presented purely for visualization purposes and does not preserve quantitative information about the phase. These two computational operations are commonly used in experimental data visualization and analysis and they are applied here as an example.

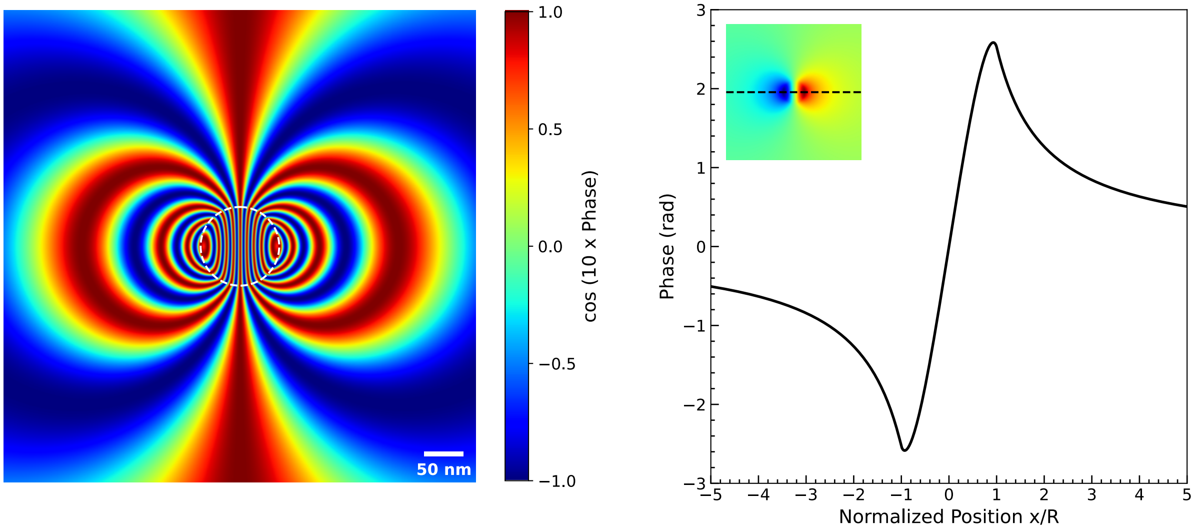

**(a)**

**(b)**

**Figure 2.5:** Phase simulation results: (a) Cosine of amplified phase (10x), to enhance the phase difference contributions. (b) Line profile perpendicular to the magnetization axis. The extracted line is showed in dashed black line in the left-upper part image.

The linear profile, extracted perpendicularly to the magnetization axis, highlights the antisymmetric nature of the phase distribution and its fast variation around the center of the sphere. The profile presents a clear maximum and minimum close to the edges of the sphere ($x_{max} \simeq 0.9R$). Beyond these extrema, the phase gradually decreases towards zero outside the object, as the distance from the center of the sphere increases. The phase difference between maximum and minimum ($\Delta\varphi_{max-min}$) is an important parameter that essentially describes the overall magnetic phase variation produced by the phase object. From Eq. 2.10 a direct relation between the phase difference and the magnetic flux is established, but this expression holds only in the ideal case of an infinite cylinder with a magnetic field fully confined inside of it. This condition is not satisfied for a uniformly magnetized sphere, where the magnetic field is not confined and electrons ideally propagate through regions in which $\mathbf{B} \neq 0$. As a consequence, phase shift is also affected by the field spatial distribution and the geometry of the finite sample, and therefore cannot be interpreted as a purely Aharonov-Bohm effect. Using the phase expression defined in Eq. 2.11 and estimating the magnetic flux of the sphere as $\phi = \pi R^2 B_0$, the expected $\Delta\varphi_{max-min}$ for a uniformly magnetized sphere can be approximated as:

$$\Delta\varphi_{max-min} \simeq \frac{4}{3}\frac{\phi}{\phi_0} \tag{2.12}$$

where the factor $\frac{4}{3}$ arises from geometrical effects and from the internal demagnetizing field of the sphere. This relation is obtained under the additional approximation that the phase maximum (and minimum) occurs at $x = R$ ($x = -R$), and is therefore treated as an approximate estimation to support the interpretation of simulations and experimental data, rather than as an exact analytical result.

To better present the fundamental properties of the phase shift produced by an uniformly magnetized sphere, a set of simulations is presented in Fig. 2.6, varying separately the radius $R$, the magnetization angle $\alpha_M$and the characteristic magnetic field $B_0 = \mu_0 M$. When one parameter is varied, the others are fixed to the previous introduced values: $R = 50$ nm, magnetization along y-axis ($\alpha_M = 90°$) and $B_0 = 1$ T.

The introduction of the magnetic moment $\mu$, defined for a uniform magnetization as $\mu = MV$ (with $V$ the volume), helps the interpretation of these simulations. The phase, described in Eq. 2.11, is proportional to the magnetic moment, which depends on both the radius and the magnetization. In Fig. 2.6, increasing the radius leads to a broader spatial distribution of the phase variation and to higher phase values, since both the volume and thus the magnetic moment grow together with radius (approximately as $\varphi \sim R^2$: this can be extracted by series expansion and evaluating the phase at its maximum). Changing the magnetization axis does not affect the phase magnitude but only the orientation in space of the dipolar shape, which remains symmetric with respect to the magnetic moment direction. Finally, changing the characteristic field modifies only the phase value and, as expected from Eq. 2.11, the phase increases linearly with the magnetic moment and so with the applied magnetization field.

By combining more than one simulated sphere, different magnetic structures can be computed by summing their single effects together. By superimposing different phase objects, therefore, it is possible to predict the phase shift of more complex systems and some useful models are reported in the following subsections.

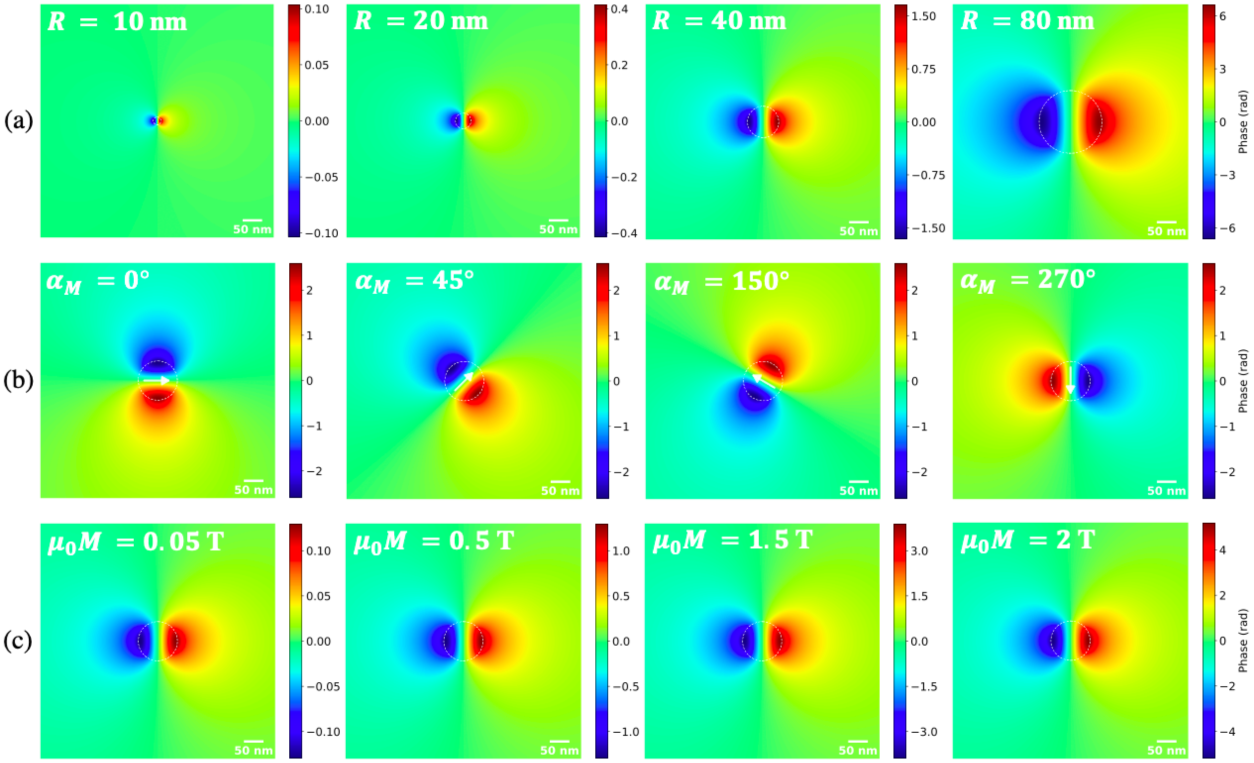

**Figure 2.6:** Magnetized sphere phase shift simulations: behavior for different fundamental parameters. (a) Radius variation. (b) Magnetization angle variation. (c) Associated magnetization variations. The field of view is kept constant to 0.6 $\mu$m. Shapes, phase scales and general behavior is strictly related to the used parameters. The white arrows point out the magnetization direction, while the white dashed lines highlight the original dimension of the simulated sphere.

### 2.5.2 Hollow sphere phase shift

Starting from a uniformly magnetized sphere of radius $R_1$ and subtracting from it a sphere with a smaller radius $R_2$ an hollow magnetic sphere is obtained. This model represents the behavior of a spherical object that contains magnetic shift sources only in its external part (with thickness $R_1 - R_2$). Hollow nanostructures are of great interest because of their high ratio of surface to volume, large pore volume and low density, which can be exploited for applications in several research fields, presenting also unique magnetic properties [34]. The simulated magnetic phases for two hollow spheres of external radius 70 nm, different internal radius (50 and 65 nm) and both generated starting from two uniformly magnetized sphere with characteristic magnetic field of 1 T are reported below, together with their line profiles, collected perpendicularly to the magnetization axes.

For what concerns the magnetic phase contribution, the simulated hollow sphere behaves like a magnetic sphere whose magnetic moment corresponds to the difference between the moments of the two spheres used to construct it. The phase maps shows a region inside the particle where the phase changes more slowly, appearing flatter and reduced compared to the filled sphere presented in Fig. 2.11. The line profiles further emphasize a smaller and less linear gradient around the center of

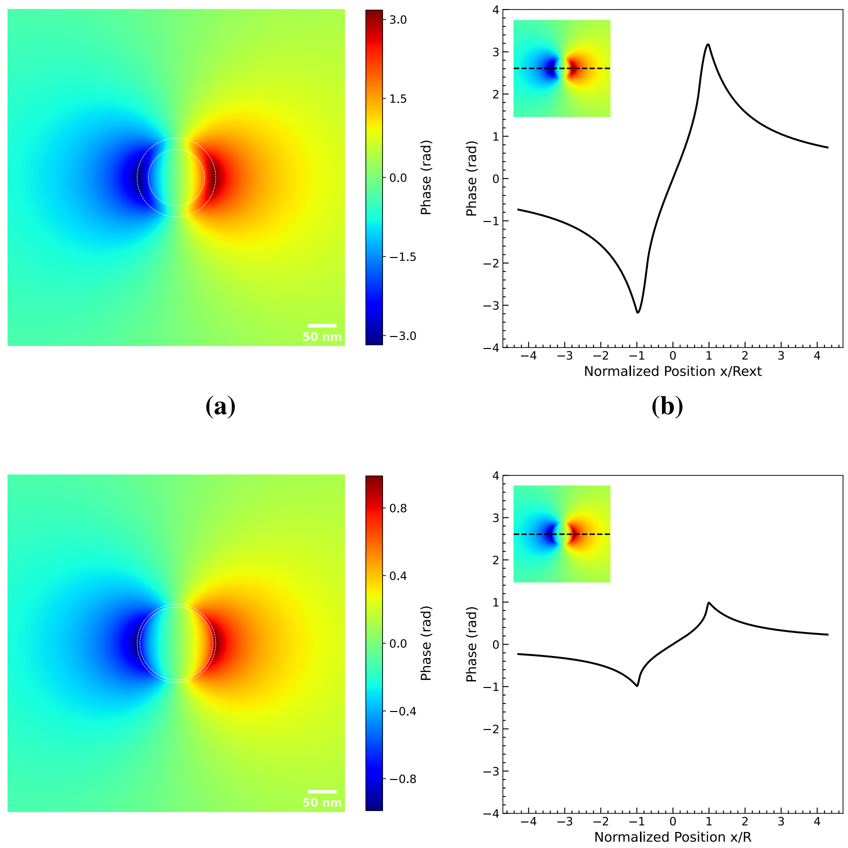

**(a)** **(b)**

**(c)** **(d)**

**Figure 2.7:** Hollow sphere simulations and line profiles in the centers perpnedicularly to the magnetization axis: two examples. (a),(b) External radius 70 nm, internal radius 50 nm, $\mu_0 M = 1$ T and field of view of 0.6 $\mu$m. (c), (d) Internal radius equal to 65 nm. The white dashed lines indicate the two original sphere boundaries. The extracted profiles are represented in the left-upper panels.

the sphere, between the maximum and minimum values, compared to the sharper variation reported in Fig. 2.5b. The obtained phase values are directly related to the thickness of the sphere and therefore to the amount of magnetic material present in the object. Outside the sphere, the phase distribution is similar to that of the filled one, whereas the main differences in behavior are observed inside the nanostructure, as discussed above.

### 2.5.3 Nanochains phase shift

Assembled structures of magnetic nanoparticles have gained interest due to their technological potential in magnetic recording media and in other research fields. In particular, chains of magnetic nanoparticles are of great interest, for example in medical applications [35] and represent a model system for investigating collective magnetic behavior emerging from dipolar interactions. In this work, linear chains of magnetic nanoparticles are modeled by arranging identical magnetic spheres side by side, each characterized by a fixed radius ($R = 20$ nm) and uniform magnetization (such that $\mu_0 M = 1$ T). In this framework, the nanochain magnetic phase shift can be computed as the superposition of single sphere contributions. This idealized scenario provides a clear and controlled way to isolate and analyze the effects of the interactions between the different magnetic dipolar contributions that create the chain. More complex and various systems can be easily designed, changing the radius, the position and the magnetization of the single constituents. Fig. 2.8 shows the simulated magnetic phase for increasing number of nanoparticles $N$ forming the chain:

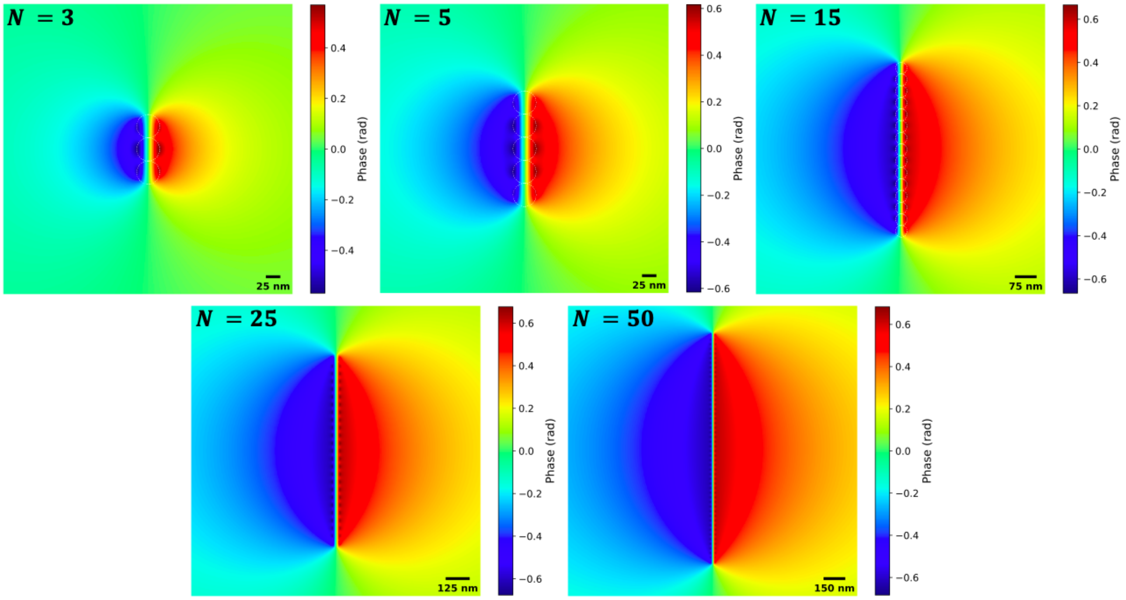

**Figure 2.8:** Nanochains phase shift simulations: obtained for different numbers of nanoparticles ($N$) arranged together. Different scales are set in order to highligth specific behavior of the phase as a function of $N$. All the spheres has 20 nm radius, $\mu_0 M = 1$ T and magnetization along y-axis.

As the number of particles increases, the individual phase contributions overlap, creating a global and uniform collective magnetic behavior. Inside the chains small single-sphere contributions (in particular at small $N$) remain visible with stronger maximum and minimum, but at higher $N$ also this signatures become a uniform phase maximum of the whole chain. This is due to the superposition of the external field of the other nanoparticles, which results in a global smoothing of the phase distribution, with a more extended and continuous behavior along the chain axis. The nanochain, when made of a high number of nanoparticles, behaves as an effective elongated magnetic dipolar object and no more as a discrete assembly of spheres.

This behavior reflects the tendency of the system to minimize its internal magnetostatic energy, through the alignment of the magnetic moments along the axis of the chain. The demagnetizing stray fields associated with the individual particles are suppressed due to the effects of the neighboring spheres. In the limit of large $N$, the system exhibits a single global stray fields extending over large distances, whose closure occurs essentially at infinity; this tendency is highlighted by the reported simulations, looking at the constant phase contours outside the chain. The described effect is encoded in the magnetic phase shift and can be visualized using the line profiles extracted perpendicularly to the chain axis in the middle region of the nanochains, where the behavior is stronger, also at lower $N$.

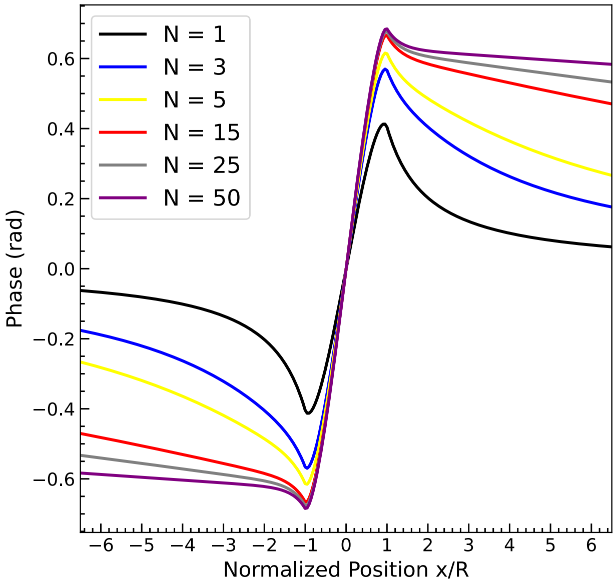

**Figure 2.9:** Nanochains linear profiles: obtained for different numbers of nanoparticles ($N$) arranged together in a chain configuration.

The profiles highlight how the extrema of the phase remain well defined as $N$ increases, maintaining the original basic magnetic behavior of single sphere. However, a significant change can be observed in the spatial decay of the phase signal. For an isolated nanoparticle ($N = 1$), the phase decreases rapidly towards zero, reflecting the effects of the dipolar field outside the sphere. As the number of particles increases, the phase profiles become progressively broader and decay toward zero occurs over larger distances. This behavior is directly related to the increasing spatial extent of the stray field that affects the phase of the electrons. In the limit of large number of particles ($N \longrightarrow \infty$) the phase no longer vanishes rapidly, but approaches a slowly varying behavior and after the peak it seems to remain constant, going to zero only at extreme distances. This reflects the global magnetic moment effects and the long-range nature of the associated stray field. As reported in literature [36], even for large $N$ the chain does not become magnetostatically equivalent to a continuous cylinder, that in the ideal case has no effects outside. For an infinite chain of spheres, the demagnetization factor remains finite, indicating the presence of the residual stray field outside the structure, which is responsible of the slow decay in the electron phase.

All the presented models provide the expected magnetic phase shift under ideal conditions and constitute qualitative and quantitative references for the interpretation of experimental data. The phase distribution encodes fundamental magnetic information and these simulations allow the identification of characteristic features of the magnetic behavior, which are crucial in the analysis carried out in this work.

## *Chapter 3*

# Phase retrieval: off-axis electron holography

The previous chapter established the fundamental role of phase in electron microscopy and highlighted the fundamental physical information it encodes. As mentioned, conventional TEM imaging provides only a partial representation of the specimen, since the recorded intensity does not directly retain the phase of the electron wavefunction. Recovering this missing phase is therefore fundamental for accessing both the electric and magnetic information at the nanoscale. To overcome the phase problem, phase retrieval method for electron microscopy must be introduced and described. A variety of approaches have been developed and they are presented in the first part of this chapter. Furthermore, since the electromagnetic fields below the nanometer scale are generally very small, another fundamental requirement is the phase resolution (precision) in a phase image. Therefore, the development of phase-sensitive techniques represents a central aspect for advance electron microscopy and is indispensable for a complete and deep characterization of materials. Within this framework, electron holography is presented as a particularly powerful experimental technique, based on wave interference, to transmit phase information into a detected intensity pattern. From the acquired interference fringes acquired, the phase of the electron wavefunction can be quantitatively reconstructed by means of a specific computation algorithm that leads to finally obtain the amplitude and the phase distributions, that can be finally analyzed. This chapter presents the theoretical basis and the practical implementation of electron holography, presenting and establishing the core of the experimental methodology employed in this work.

## 3.1 Phase microscopy techniques

Several approaches have been developed to overcome the phase problem in electron microscopy and to access or retrieve the phase of the electron wave from intensity measurements. This research field is, in general, known as phase microscopy and includes a variety of techniques, which are subdivided into different categories depending on how the phase information is encoded into the measurable quantities.

- **Phase contrast methods**:
  In conventional imaging (considering an ideal microscope) objects induce only phase mod-

ulation, which are not directly observable in intensity. For this reason, different techniques are implemented in order to transfer information (encoded in the phase) inside the visible amplitude. This is the framework of Contrast Transfer Function Theory, in which phase modulations are converted into measurable intensity through the effects of the imaging system. Lens aberrations and defocus introduce relative phase shifts between the electron beams, interference and phase shifts in image plane. Moreover, additional phase shifts can be introduced by apertures or phase shifting elements (phase plates). The specific contribution of each optical element to the final image formation can be described analytically (using transfer function), allowing the design of specific imaging conditions to control the information transfer. Representative examples include Fresnel (out of focus) imaging and Zernike phase contrast (adding specific phase plates) [2, 12].

- **Interferometric methods**:
  Interferometric techniques provide direct access to the phase by superimposing electron wave with a coherent reference one. They are not based on contrast transfer function and encode phase information directly in interference fringes of the produced interference pattern. Starting from the acquired pattern, phase and amplitude can be extracted using specific reconstruction procedures, generally based on Fourier methods. Electron Holography is the most important and adopted interferometric technique and will be presented in detail in the following sections [23].

- **Differential/STEM methods**:
  In scanning-based approaches, phase information is extracted from the measurement of beam deflection induced by local electromagnetic fields in the sample, which are directly related to phase gradients. Differential Phase Contrast (DPC) is the principal technique based on this concept and relies on the measurement of the shifts in the diffraction pattern caused by the specimen. DPC provides, using the shifts, direct access to the gradient of the phase, which can be integrated to obtain the phase distribution. Since a localized probe is required, these methods are typically implemented in STEM mode [37].

- **Phase retrieval computational methods**:
  These techniques reconstruct the phase starting from intensity-only measurements by solving an inverse problem. An important approach is based on through-focus series, applied for example in Transport of Intensity Equation (TIE), which relates intensity variation along the optical axis to the phase distribution [38]. Other methods include and are based on iterative algorithms to recover the phase (for example the Gerchberg-Saxton or the Fienup input-output algorithms [39, 40]), solving the inverse problem, such as ptychography or other tomography techniques [41, 42].

Each of these techniques presents specific advantages and limitations in terms of experimental complexity, resolution and quantitative accuracy. Among them, electron holography provides a direct and quantitative measurement of the phase and is therefore particularly suitable for the investigation of electrostatic and magnetic fields in transmission electron microscopy. For this reason, it is adopted as the primary technique in this work.

## 3.2 Off-axis electron holography

### 3.2.1 Historical background

In 1948, the Hungarian physicists Dennis Gabor designed in-line electron holography as a new technique to improve the resolving power of the electron microscope and to correct for lens aberrations [43]. Gabor's method aimed to collect the complete wave with amplitude and phase, after the interaction with the system, by interfering the propagated object wave with a known reference wave. The arising interference fringes were modulated in contrast and position by amplitude and phase of the wave, respectively. In this way a complete interference pattern was recorded and he named it 'hologram', because it encoded everything (from Greek *holos* + *graphe*, meaning 'complete writing). Practical implementation of this approach was initially limited by electron source coherence of available sources and reconstruction problems from the object wave starting from the interference pattern. Gabor's technique is known as in-line holography because the reference wave and the object one propagate in the same direction; the experimental realization and the reconstruction process for this method were developed in 1962 by Leith and Upatnieks [44].

Starting from this idea, Möllenstedt and co-workers developed off-axis electron interferometry in 1954, using an electrostatic biprism to split and recombine electron waves. In this method the reference and object waves interfere, reaching the detector plane with different slight angles. The first off-axis electron hologram was recorded and successfully reconstructed in Germany using lasers light, treating the interference pattern as a diffraction grating, in 1968 by Möllenstedt and Wahl [45]. In the late 1960s, Tonomura further established this technique as a practical and quantitative technique through improved stability and phase reconstruction [46]. With advances in electron source coherence and TEM instrumentation, off-axis electron holography became the most successful and widespread holographic method applied in electron microscopy, enabling high quality studies of electron phase at the nanoscale and with nanometer resolution. Today, off-axis electron holography represents a fundamental tool in materials science and nanotechnology, enabling direct visualization of electromagnetic fields and internal potentials that are otherwise inaccessible through conventional imaging techniques [25, 23].

Holography invention and development led Gabor to win the Nobel Prize in Physics in 1971 [47]. Furthermore, this technique also played a role in verifying important quantum phenomena and one of the most important experiment was the 'observation of the Aharonov-Bohm effect' (presented in Section 2.4). In 1982, using off-axis electron holography Tonomura et al. recorded interference patterns around toroidal ferromagnets, showing that electrons acquire a phase shift due to enclosed magnetic flux also when they travel in field-free regions [48]. This work confirmed that vector potentials have physical consequences and can be considered real quantities. Other relevant results obtained by using electron holography regards the quantitative mapping of magnetic fields (domains), electrostatic potentials and charge distributions at the nanoscale [49] and also the characterization of flux vortices in superconductors [50].

### 3.2.2 Hologram formation

Off-axis electron holography is based on the interference, produced by a biprism, of coherent electron waves. To understand how the hologram is generated, the role and the effects of the biprism need to be presented.

**Electron biprism**

The electrostatic biprism, introduced in 1955 by Möllenstedt and Düker [51], consists of a conductive filament electrode placed between two grounded parallel-plates electrodes. It is generally made of a metal-coated glass fiber wire with a typical diameter of 1 $\mu$m or less, located in the selected area aperture plane of the column (as presented in Fig. 3.1). When a voltage $V_B$ is applied to the filament, an electrostatic field is generated and it separates the incident electron beam into two electron beams, which are then linearly deflected in divergent or convergent direction, depending on the applied potential sign. This results in the overlap of two coherent parts of wave, leading to the formation of an interference pattern in the image plane. By applying a positive potential the two split electron beams are deflected in converging direction interfering near the optical axis (Fig.3.2a). The biprism can be approximated as an infinite cylindrical capacitor and its interaction with the electron beam can be modeled. The deflection angle $\alpha$ of the electron beams is proportional to the biprism applied voltage $V_B$ and depends on both the characteristics of the beam and on the biprism geometrical parameters:

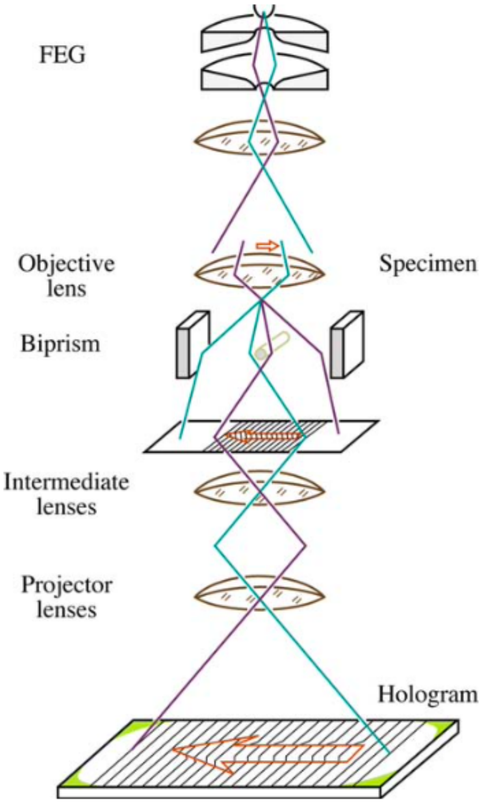

**Figure 3.1:** Operation of a biprism in TEM column: interference pattern creation.

$$\alpha = \frac{\lambda V_B C_E}{2\log\left(\frac{R_g}{r_B}\right)} \tag{3.1}$$

where $r_B$ is the filament radius, while $R_g$ is the distance between the filament and the grounded plates. Furthermore, the fringe spacing $L$ in the interference pattern is inversely proportional to the biprism voltage:

$$L = \frac{\log\left(\frac{R_g}{r_B}\right)}{V_B C_E} \tag{3.2}$$

These two equations highlight the strong dependence of interference pattern characteristics on the applied voltage and on the geometrical and beam properties, which are of fundamental importance for optimizing the experimental conditions during the electron holography experiments [2, 25, 52].

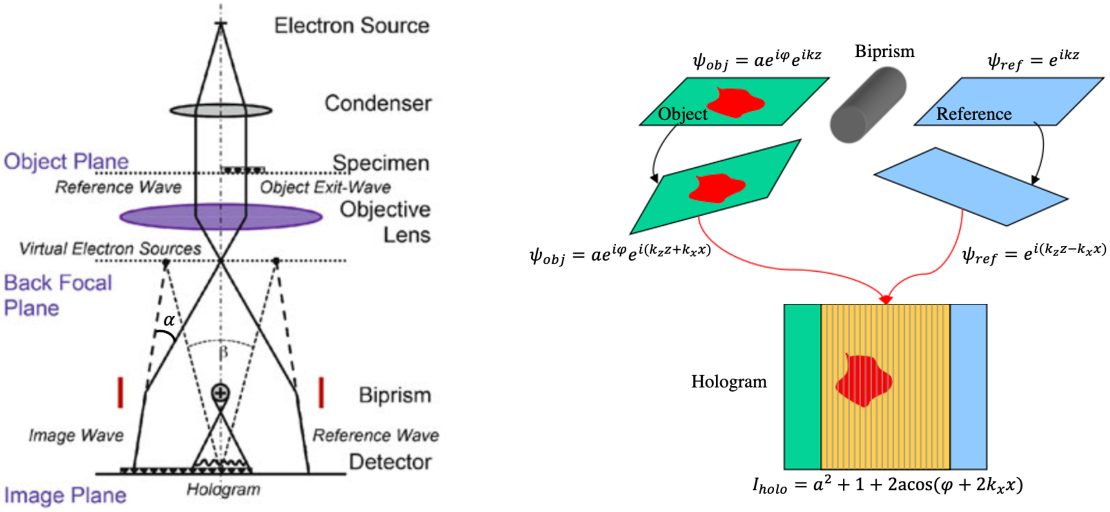

**(a)** **(b)**

**Figure 3.2:** Electron holography sketches: (a) Holography set up and electron beams path: the sample and a vacuum region are illuminated by a plane electron wave. In this way a modulated object exit wave and an unmodulated reference one are created. By means of a positive biased biprism both waves are deflected towards each other, resulting in two virtual electron source in the back focal plane of the objective lens. The two deflected wave are brought to overlap forming the electron hologram (interference pattern between the object wave and the reference one) on the image plane. (b) Hologram formation: the object and the reference waves, applying a voltage to the biprism, are deflected and then interfere, creating the hologram. The hologram presents the overlap region with clear interference fringes that cover the object and its intensity can recorded at the detector plane.

The ideal configuration to collect an hologram is the one in which the electron wave after the interaction with the sample is made of a part of electrons that has interacted and is phase modulated and a part that has traveled in a 'vacuum' region (region without the sample) separated in space as presented in Fig. 3.2a. Then the object wave, traveling along z-axis, encounters the biprism and is split in two plane wave parts, the one coming from the vacuum region is the reference wave $\psi_{ref} = e^{ikz}$ (for simplicity the amplitude of the reference is considered one) and the one coming from the interaction with sample is the modulated object wave $\psi_{obj} = ae^{i\varphi}e^{ikz}$, with $a$ the amplitude and $\varphi$ the phase. These two plane waves are deflected by an angle $\alpha$, given by Eq. 3.1, obtaining two deflected plane waves $\psi_{ref} = e^{i(k_z z - k_x x)}$ and $\psi_{obj} = ae^{i\varphi}e^{i(k_z z + k_x x)}$, with different signs in

$k_x$ because of the opposite deflections, $k = \sqrt{k_z^2 + k_x^2}$, $k_x = k \sin\alpha$ and $k_z = k \cos\alpha$. The two deflected waves interfere and the intensity recorded by the detector is:

$$I_{holo} = |\psi_{ref} + \psi_{obj}|^2 = a^2 + 1 + 2a\cos(\varphi + 2k_x x) \tag{3.3}$$

where it is evident that phase information is encoded in this amplitude equation and the phase problem can be considered solved by means electron holography. The hologram intensity is made of three separate contributions: the object image intensity, the reference image intensity (a uniform background) and a set of cosinusoidal fringes, with local phase shifts and amplitudes equivalent to the ones of the electron wavefunction in the image plane, respectively. The final result is an image with an overlap region with interference fringes that cover the object (Fig. 3.2b) [21, 23, 26].

## 3.3 Phase reconstruction in electron holography

Once the hologram with its intensity expressed by Eq. 3.3 is obtained, the aim is to recover the image wave from it. To do this, numerical image processing is performed according to wave optical laws. This reconstruction method consists of three fundamental steps and is generally named Fourier transform method [44], because it is based on specific operations in Fourier space, or hologram reconstruction method.

### 3.3.1 Hologram reconstruction method

**Step 1 - Fourier transform of the hologram**:
The Fourier spectrum of the hologram is evaluated, obtaining a diffractogram (for simplicity $k_x = k$):

$$\mathcal{F}[a^2 + 1 + 2a\cos(\varphi + 2kx)] = (a^2 + 1)\delta(q) + a\mathcal{F}[e^{i\varphi}]\delta(q - 2k) + a\mathcal{F}[e^{-i\varphi}]\delta(q + 2k) \tag{3.4}$$

obtained by splitting the cosine through Euler's formula, applying Fourier Transform (FT) to the single terms and using the Dirac delta definition. Defining the phase object spectrum function as $s(q) = \mathcal{F}[e^{i\varphi}]$, the product between this function and the Dirac delta can be interpreted as a convolution, in which the $\delta$ function translates the center of the $s$ function in its center. In this way, the diffractogram becomes:

$$\mathcal{F}[a^2 + 1 + 2a\cos(\varphi + 2kx)] = a[s(q - 2k)] + (a^2 + 1)\delta(q) + a[s^*(q + 2k)] \tag{3.5}$$

revealing 3 separated bands (peaks) on a background. The center band ($(a^2+1)\delta(q)$) that represents the conventional image, involves only intensities and does not contain phase information, therefore this is not of further interest in this context. The two sidebands ($a[s(q \pm 2k)]$) contain the Fourier spectrum of the complete image wave convoluted around ±$2k$, hence encode all the information of the object wave and they are the quantities of real interest. The two sidebands carry, by symmetry, exactly the same information.

**Step 2 - Mask out one of the two sidebands and centering**:
Using a numerical aperture, one of the sidebands (the positive) is selected and the origin of the Fourier space ($q = 0$) is redefined by moving the mask around it, centered on the pixel with maximal value. With this translation in Fourier space the $s$ function is no longer shifted of $2k$ and represents the spectrum of the recorded image wave.

**Step 3 - Inverse Fourier transform of the centered sideband**:
With this final step, coming back in real space, amplitude and phase of the wave after the interaction with sample is directly extracted:

$$\mathcal{F}^{-1}[as(q)] = F^{-1}[a\mathcal{F}[e^{i\varphi}]] = ae^{i\varphi} \tag{3.6}$$

Amplitude and phase are reconstructed and they are directly obtained, without being mixed with different quantities, and can be easily plotted and analyzed.

Holography is extremely sensitive to any bending of interference fringes and these effects have to be taken into account within the reconstruction process. In general, reconstructed phase can present artificial phase structure related to geometric distortions due to lenses or CCD-camera, charging effects or biprism defects. Additionally, mistilt of the reconstructed wave may be introduced by improper centering of sideband at step 2. Therefore, for each hologram, an empty reference hologram $I_{empty}$ is recorded in the same optical parameters, but without object and its reconstructed wave is used for corrections of artifacts and mistilt and for normalization of the reconstructed amplitude. In practice, the correction is possible by performing a complex division of the reconstructed object wave function by the empty reference reconstructed wave function in real space. The phase extracted from this ratio will be normalized in amplitude and distortion-free and for this reason it can be considered more representative of the object wave phase and used for quantitative analysis and interpretation. [23, 21].

### 3.3.2 Phase and amplitude - interpretation and analysis

By means of the presented algorithm, the phase and the amplitude of the electron wave function are retrieved. In particular, the two quantities of interest are analytically extracted from complex numbers (with real part $Re$ and imaginary part $Im$) that result from the division by the empty reference hologram. Amplitude and phase are respectively computed as $a = \sqrt{Re^2 + Im^2}$ and $\varphi = arctan(\frac{Im}{Re})$.

**Reconstructed amplitude**

In general, the reconstructed amplitude is similar to an energy-filtered bright-field TEM image, since the contribution of inelastic scattering to holographic interference fringe formation is negligible [26, 53].

**Phase unwrapping**

In general, the phase is the most interesting part and, as mentioned, it is extracted by means of the arctan function. For this reason, the reconstructed phase, after the algorithm, is displayed in the range $[0, 2\pi]$, but in presence of strong phase objects, this retrieved quantity can exceed $2\pi$ creating unwanted phase jumps from zero to $2\pi$ wherever the phase $2\pi$. This wrapped phase distribution show up the equiphase lines and gives an instructive overview of the phase behavior for a first visual interpretation. Before a detailed quantitative analysis, the discontinuities have to be removed by means of a phase-unwrapping procedure [54], which adds or subtracts $2\pi$ at the phase jumps locations, in order to visualize the true phase values. The basic effect of the unwrapping strategies are reported in Fig 3.3b applied to a simulated generic gaussian signal. [23, 55].

**Separation of phase contributions**

As described by Eq 2.6, the measured and holography reconstructed phase is always the sum of the electrostatic and the magnetic contributions. To perform specific analysis, these two components need to be separated. A fundamental strategy have been developed and it consists of taking two holograms of the same sample with a reversed sign for $\varphi_{mag}$. The phases of the two holograms will be $\varphi_1 = \varphi_{el} + \varphi_{mag}$ and $\varphi_1 = \varphi_{el} - \varphi_{mag}$. From the acquisition and reconstruction of the two phases, the electric and magnetic part can be separated as:

$$\varphi_{el} = \frac{\varphi_1 + \varphi_2}{2} \tag{3.7}$$

$$\varphi_{mag} = \frac{\varphi_1 - \varphi_2}{2} \tag{3.8}$$

The magnetic phase inversion operation, from the experimental point of view, can be realized in many different ways, depending on the sample and the available instrumentation. Possible approaches are to physically flip the specimen, to reverse the magnetization (applied field) of the sample, to subtract the electrostatic phase (evaluated from the thickness by means of Eq. 2.7) or to tilt the sample [56].

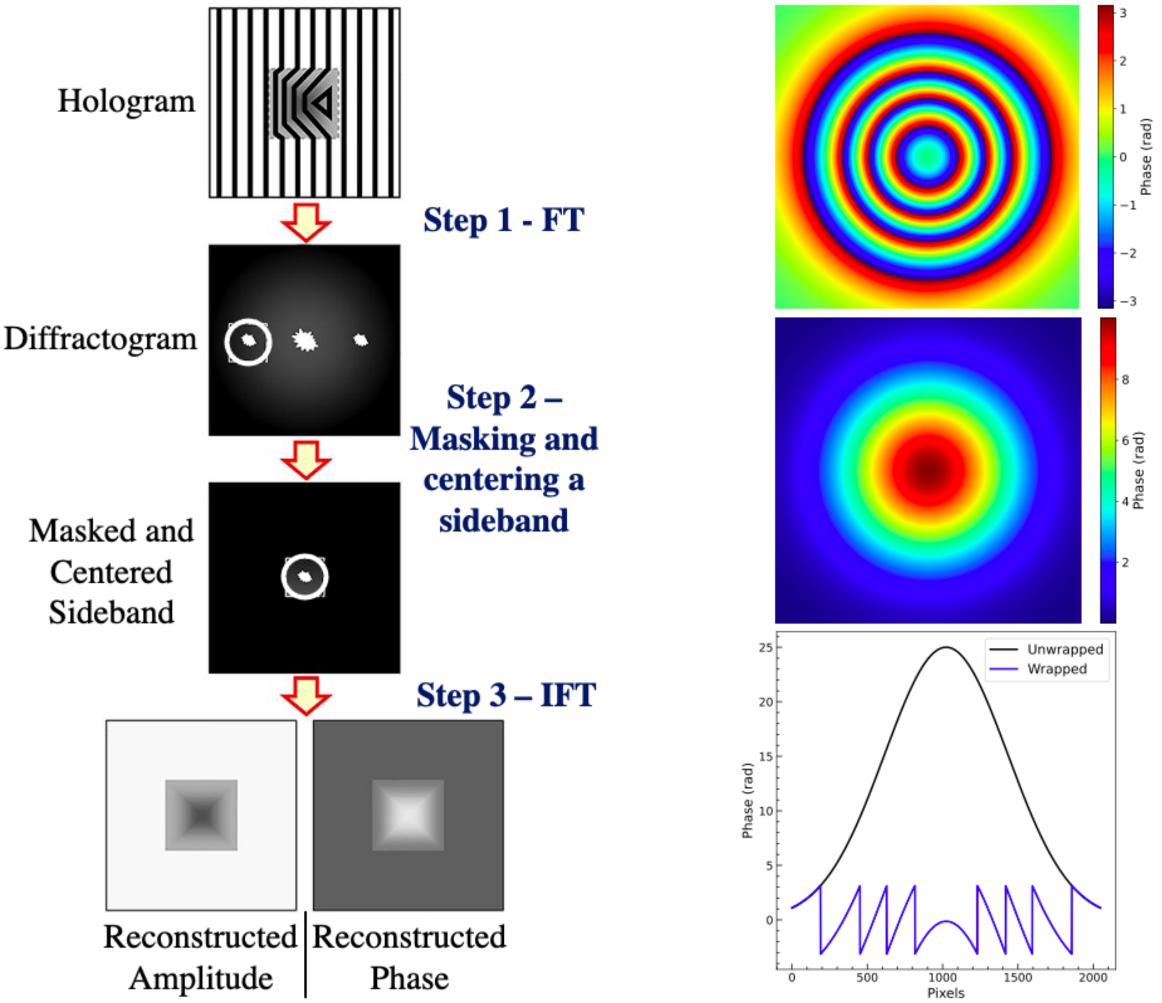

**(a)** **(b)**

**Figure 3.3:** (a) Reconstruction method in electron holography: representation of the 3 steps to recover amplitude and phase. (b) Simulation of wrapping effect on gaussian phase: simulation of a wrapped gaussian phase. In the upper image the wrapped phase, with discontinuities between $-\pi$ and $\pi$. In the middle the unwrapped phase, using the unwrapping algorithm the original gaussian behavior is reconstructed, with no more jumps in limit values. In the lower image a linear profile is reported, emphasizing the discontinuities of the wrapped phase with respect to the uniform original and expected behavior.

# *Chapter 4*

# Characterization of magnetic FeCo nanoparticles

In this chapter samples are presented and the experimental analysis is carried out, starting with a complete description of the holography reconstruction algorithm and arriving to the final and complete extraction of the magnetic properties of the studied structures.

## 4.1 Magnetic $Fe_xCo_yO_z$ nanoparticles and nanochains

### 4.1.1 Nanostructures sample presentation

Magnetic nanoparticles have attracted significant attention over the past decades due to their unique size-dependent magnetic properties, which differ from their bulk counterparts. Reduced to nanoscale, ferromagnetic and ferrimagnetic materials can exhibit single-domain behavior, superparamagnetism, and enhanced surface-to-volume ratios, making them highly tunable for a wide range of applications. Recent research has increasingly focused on the controlled assembly of more than one nanoparticles, to form one-dimensional architectures such as magnetic nanochains. These nanostructures can be synthesized spontaneously under external magnetic fields or via template-assisted synthesis. The resulting chain-like morphology introduce magnetic behaviors leading to properties that cannot be achieved in individual nanoparticles. Thanks to their particular properties nanochains find applications in many technological fields [35, 7].

The experimental investigation presented in the experimental part of this work is devoted to the magnetic characterization of nanoscale systems. The samples analyzed in this work were synthesized by external research groups and provided within the framework of a wider interdisciplinary research collaboration. This project involves the TEM group of the University of Modena and Reggio Emilia and CNR-NANO, the department of Chemistry and Industrial Chemistry (DCCI) of the University of Genova and... chi altro?...

The investigated nanostructures can be classified into two main categories: nanoparticles (NP), which exist either as isolated entities or as aggregated ones creating more complex clusters, and nanochains (NC), synthesized as sequences of interconnected nanoparticles arranged in chain-like shape. A first TEM image of the two samples is reported in Fig 4.1

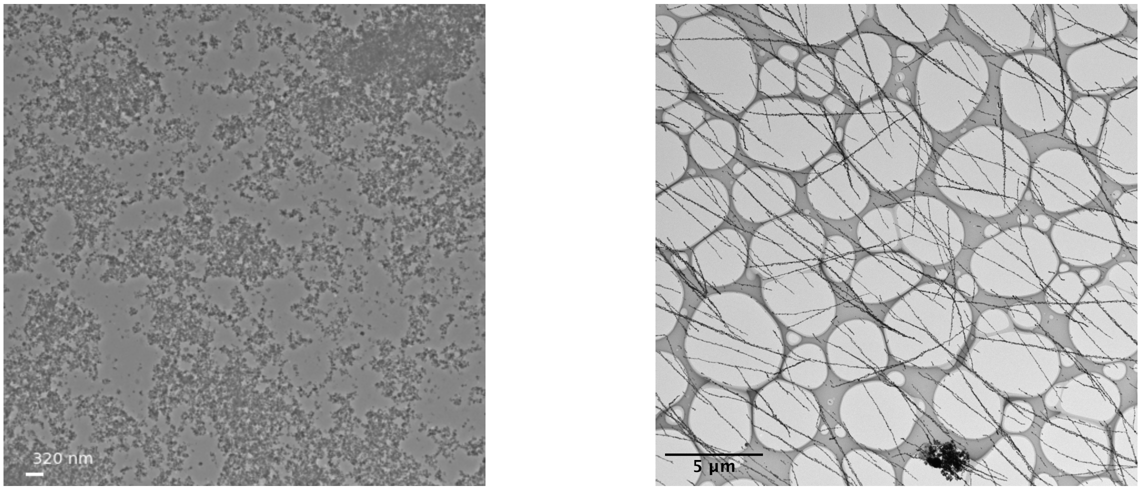

(a) (b)

**Figure 4.1:** First TEM images of the samples: (a) Nanoparticles (b) nanochains

The provided magnetic Cobalt Ferrite nanoparticles find applications in biomedical sector biomedical sector [8] and in many other fields. Magnetic Iron-Cobalt (FeCo) nanochains by means of their special properties find applications for example in Electromagnetic wave absorption and microwave shielding [10], flexible devices and sensors [11].

In the framework of this wide research field, these samples have been provided in order to characterize their magnetic behavior and properties at the nanoscale. Five different samples were delivered at different times and within the framework of distinct research projects. All the known information about them are presented below:

- **Sample SI88 - Cobalt Ferrite nanoparticles - A (NP-A)**:
  $Fe_{2,25}Co_{0,75}O_4$. Characterized by the producers: Saturation magnetization $M_s \simeq 99$ Am$^2$/Kg, Residual magnetization $\frac{M_r}{M_s} \simeq 0.54$, Crystalline size $D_{XRD} \simeq 28$ nm
- **Sample SI90 - Cobalt Ferrite nanoparticles - B (NP-B)**:
  $Fe_{2,75}Co_{0,25}O_4$. Characterized by the producers: Saturation magnetization $M_s \simeq 82$ Am$^2$/Kg, Residual magnetization $\frac{M_r}{M_s} \simeq 0.44$, Crystalline size $D_{XRD} \simeq 31$ nm
- **Cobalt Ferrite nanoparticle cluster - C (NP-C)**:
  $Fe_2CoO_4$
- **Iron Cobalt nanochains - A (NC-A)**:
  FeCo. Not oxide.

### 4.1.2 TEM specimen preparation

The nanoparticles samples were provided in powder form and hence subsequently dispersed into isopropanol to obtain a suspension. Due to their magnetic nature, the particles tend to aggregate together forming big clusters/aggregates. In order to observe and analyze this system at the nanoscale, it is necessary to achieve good dispersion with well separated particles and without the presence of micro-scale (or bigger) agglomerates. Therefore, to avoid this problem and to allow easier TEM measurements, the suspensions were sonicated in an ultrasonic water bath for approximately 40 minutes. The combination of acoustic vibrations and thermal-induced agitation leads to the breakdown of particles aggregates, improving the dipersion. After the sonication, the suspensions are deposited, by drop casting, onto the TEM grids (we used commercially available copper grids from TedPella with a $\sim 10-15$nm thick membrane of amorphous carbon on top). The solvent evaporates under ambient conditions, leaving the nanoparticles distributed on the grid surface. Finally, the samples are treated using plasma cleaner, removing surface contaminations and minimizing hydrocarbon deposition by means of the action of a low pressure plasma (made of a mixture of oxygen and argon), created by the application of an electric field to the gas, that chemically and physically clean the surface of the grids. This last step improves the quality and reduce the contamination during the TEM analysis.

Differently from nanoparticles, the nanochains samples were sent already deposited on TEM grids (a commercially available copper grid with Lacey carbon on top) and stored in a Nitrogen Glovebox isolated from external environment in order to prevent oxidation.

## 4.2 Experimental TEM setup and acquisition conditions

### 4.2.1 TEM - TALOS F200S

The TEM used to carry out our experiment is a Thermo Fisher TALOS F200S equipped with a 200 kV Schottky-FEG Electron Source (with characteristics halfway between these two types of electron gun presented in Section 1.3.1). For what concerns detectors, this instrument presents a CCD camera (TFS CETA camera), which is a scintillator-based TEM camera that uses a scintillator layer to convert incoming electrons into visible light. The light is then guided via optics fibers onto a CMOS (complementary metal-oxide-semiconductor) sensor (shown in Fig. 1.9a). The samples are placed into a Single tilt side-entry holder. The whole microscope is controlled by means of a specific TEM software. To perform holography this microscope presents both a birpism in its Selected Area Aperture Plane and an additional lens below the objective lens called Lorentz lens.

### 4.2.2 Lorentz lens

A Lorentz lens is a special TEM lens, which is not available in all TEMs, that allows to image magnetic structures in field free condition, i.e. with the objective lens off and so without any applied magnetic field to the sample. It can be considered as the objective lens operating in a low or near zero magnetic field mode. In field free condition the objective lens is turned off is also called Lorentz mode and in this configuration or weakened and a different lens (the objective mini-lens or a dedicated Lorentz lens) is activated in imaging, creating a low-field region around the sample. This is important because, otherwise, the strong magnetic field of the objective lens would destroy the magnetic structure of the material [21].

### 4.2.3 Imaging acquisition conditions

To perform standard imaging in TEM, the beam is aligned, the condenser lens system is adjusted to obtain the right illumination, astigmatism correction is performed using stigmators ( condenser stigmator to optimize the illumination and objective stigmators to optimize the acquisition), the sample is brought to focus and imaged at the required magnification and exposure conditions (electron dose and exposure time) are set. For HRTEM imaging the beam is accurately aligned and adjusted to be parallel, astigmatism is corrected, and then at high magnifications the objective lens is tuned to reach the scherzer focus for optimal contrast. In high resolution imaging high thermal and mechanical stability are necessary [2].

### 4.2.4 Holography acquisition conditions

To carry out the Holography experiments Lorentz Mode is used. Standard alignment and correction are performed and then the biprism is inserted. In off-axis electron holography the main focus is on the interference pattern formed by the superposition of the object and the reference waves. In particular, the quality of the hologram is determined by the visibility of the interference fringes, hence by the difference between maximum and minimum (i.e., the fringe contrast) in the intensity distribution. Therefore, the fringe contrast, in holography, is more important than the intensity and it is commonly used to quantify and control hologram quality. The contrast is defined as:

$$C = \frac{I_{max} - I_{min}}{I_{max} + I_{min}} \tag{4.1}$$

To achieve high fringe contrast, the illumination conditions are optimized to maximize the spatial coherence of the electron beam. Generally, to keep contrast high the illumination is tuned to be strongly astigmatic (elliptical), perpendicularly to the biprism, the $C2$ lens is strongly excited, creating a more collimated beam, biprism voltage is set to obtain well defined fringes and the time exposure is controlled, to increase the electron dose on the sample [23].

In the performed measurements, the fringe contrast is consistently maintained always above 20%, the biprism voltage is set to $V_B$ = 140 and 150 V and the exposure time is fixed to 4 s.

After identifying a nanostructure of interest in the sample, it is placed in the middle of the field of view. The electron biprism is then adjusted so that the interference region is properly aligned with respect to the structure, and the hologram is acquired. In order to ensure identical acquisition conditions, a reference hologram is rapidly acquired in a vacuum region of the sample, immediately after the sample hologram acquisition.

## 4.3 Morphological characterization

The samples are first morphologically examined by means of TEM and HRTEM imaging. Different images at various magnifications are acquired and presented in this section, in order to describe and understand the basic distributions and characteristic of the specimens.

### 4.3.1 Morphology and structure of NP-A sample

From the TEM image in Fig. 4.2 two clusters of these nanoparticles are presented. From these images single particles are evident and their typical radius can be approximated between 20 and 50 nm. In the pictures the single structures can be individuated and in some cases can be also found isolated. In this framework, after sonication for long time the aggregate can disintegrate, with the following separations of single magnetic nanoparticles.

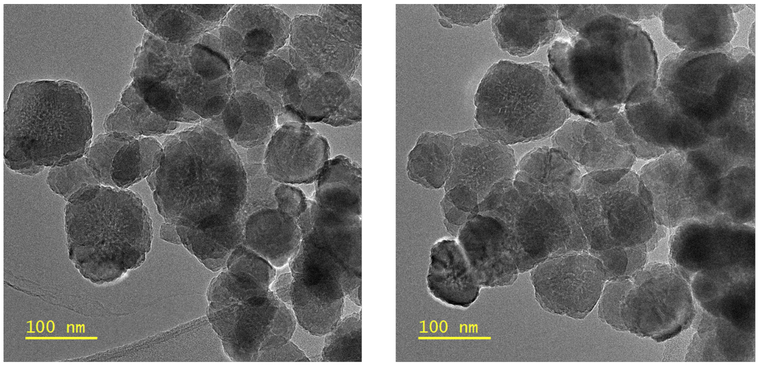

**Figure 4.2:** TEM image of Cobalt Ferrite nanoparticles NP-A.

In Fig. 4.3 some high resolution imaging are shown. Significant crystalline contributions are clearly visible and the nanoparticles seem to be formed by singles crystal and not by aggregates of smaller nanostructures. Here HR-TEM highlights the crystalline planes and provides important morphological information of this systems at the nanoscale. It is possible to conclude that this sample presents agglomerated structures formed by separated nanoparticles, most likely formed by single crystal, with a quite rough surface.

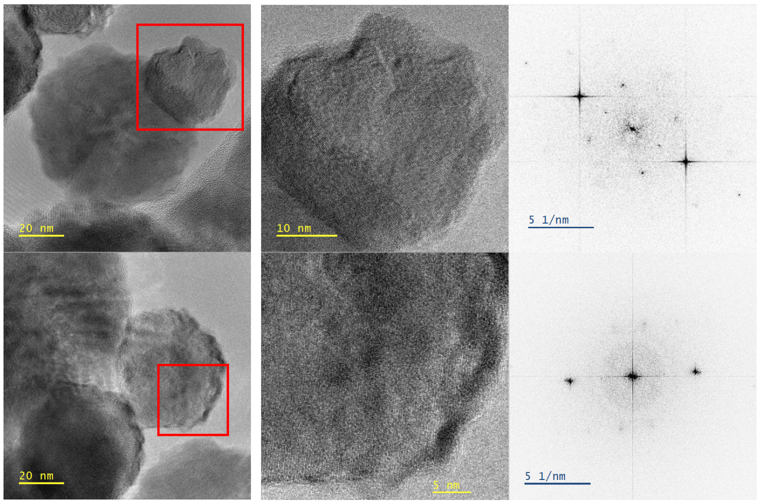

**Figure 4.3:** HRTEM images of Cobalt Ferrite nanoparticles NP-A.

### 4.3.2 Morphology and structure of NP-B sample

The TEM and HR-TEM images of this sample present similar features with respect to the NP-A specimen, with clear nanoparticles aggregates, with rough surfaces and crystalline behaviors. The nanoparticles appears as single monocrystals. The diameters of the particles is variable, but in this sample an higher number of smaller radius nanostructures are present.

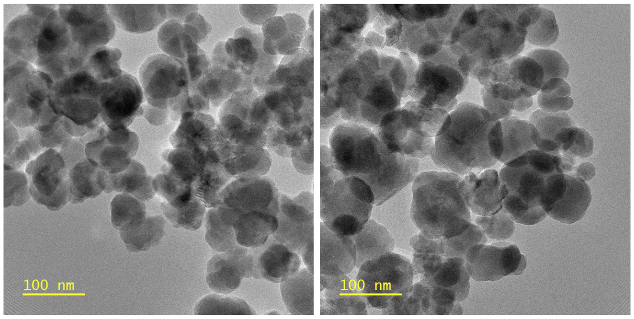

**Figure 4.4:** TEM images of Cobalt Ferrite nanoparticles NP-B.

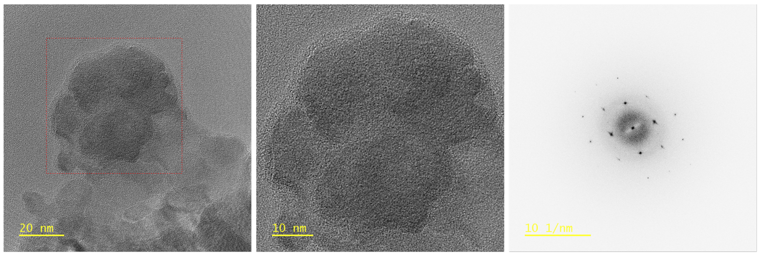

**Figure 4.5:** HRTEM images of Cobalt Ferrite nanoparticles NP-B.

### 4.3.3 Morphology and structure of NP-C sample

The cobalt ferrite nanoparticle cluster presents a quite different structure with respect the one presented for the two previous samples. From low magnification images (Fig 4.6) The nanoparticles again are found subdivided in aggregates, where the general radius of the single structure is between 20 and 50 nm. The appearance is different from the two Cobalt Ferrite samples and presents several smaller features inside the nanoparticles, with smaller radius and peculiar structures. For this reason and also from the observation on the HR image this sample presents the features of an aggregate of quite smaller nanoparticles (with typical radius around 10 or smaller). The high resolution images is also characterized by a less crystalline structure if compared with the other two nanoparticle samples.

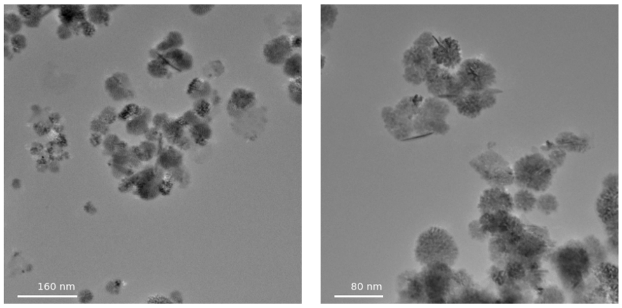

**Figure 4.6:** TEM images of Cobalt Ferrite nanoparticles NP-C.

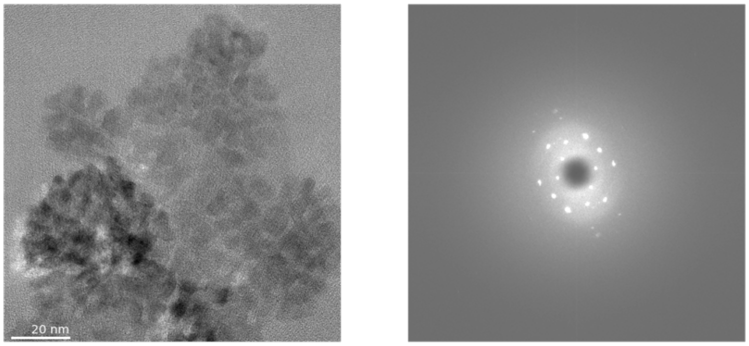

**Figure 4.7:** HRTEM image of Cobalt Ferrite nanoparticles NP-B.

### 4.3.4 Morphology and structure of NC-A sample

The nanochains sample presents an elevated number of chains, distributed on the grid with a very high density. The single particles that form the chains has radius comparable with the ones measured before for the other samples. The length of a single chain is elevated and only a few samples enters in the field of view, also at this small magnfication. For this reason it will be not easy to find isolated nanochains a higher magnifications. Chains are HRTEM is not performed on this sample.

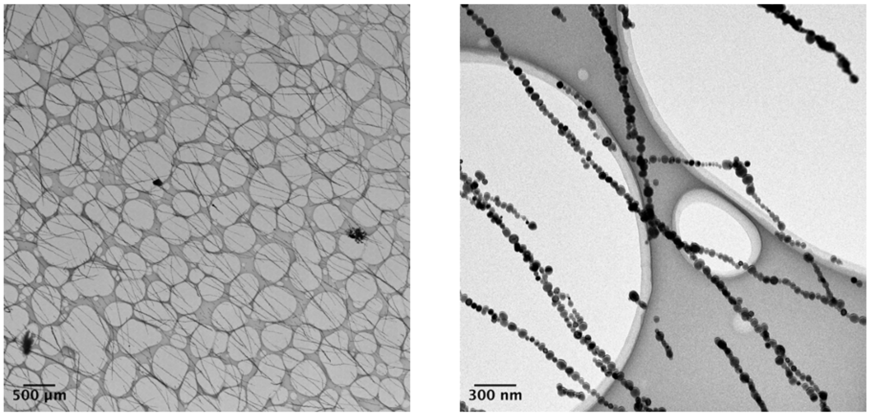

**Figure 4.8:** TEM images for iron cobalt nanochains NC-A.

Morphologic analysis helps in understanding dimensions, surface and other structural properties of materials, but with this techniques magnetic signals can't be visualized and for this reason other methods needs to be implemented, such as electron holography, in order to reconstruct the phase of the sample, and therefore their magnetic contributions.

## 4.4 Off-axis electron holography on magnetic nanostrucutres

After each measurement session, several holograms were acquired from different samples. As shown in Section 3.3.2, the extraction of magnetic contributions requires two holograms for each nanostructure: one acquired in the initial orientation and one after flipping the sample. However, finding the same nanoparticles after flipping is a challenging task, since it requires to individuate and recognize structures with flipped shapes and nanometric details over relatively large areas. For this reason, not all the acquired data could be successfully re-identified after flipping and therefore a subset of the recorded holograms does not have a corresponding flipped counterpart. Consequently, the magnetic (or electric) phase cannot be reconstructed for these cases with holography. The other holograms, together with their flipped counterparts, can be fully reconstructed and the magnetic phase can be subsequently analyzed in order to characterize the magnetic behavior of the samples.

The error on each measurement and analysis is evaluated and discussed in depth. Simulations play a crucial role in this work, as they constitute an essential reference for qualitative and quantitative comparison with the experimental results.

### 4.4.1 Phase reconstruction procedure on a representative nanoparticle

When, after the flipping operation, a nanostructure is re-identified, its hologram is acquired and the phase reconstruction procedure can start. The acquired images have dimension $D \times D = 4096 \times 4096$ x 4096, generally with a pixel size $p_{in} = 2.634 \times 10^{-10}$ m. Each couple of holograms undergoes the following set of computational operations. In this section, the standard analysis is applied to a nanostructure with two side by side nanoparticles of the sample NP-A, reported in Fig. 4.9.

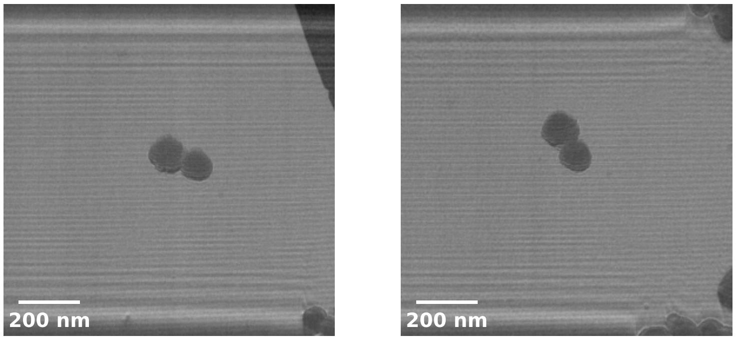

**Figure 4.9:** Two acquired holograms for the same nanostructure (NP-A1), original on the left and flipped on the right.

1. **Cropping, rotation, flipping and alignment**:
   The first operations performed on the two holograms are aimed at making them directly comparable and spatially superimposable; this is a necessary condition for reliable phase reconstructions. To this end, a sequence of basic geometric transformations are applied to the holograms. First, a region of interest is selected by cropping part of the original field of view, reducing the images dimensions, removing irrelevant features and isolating the structure of interest. In addition, cropping helps the subsequent processing steps, by reducing computational costs, since the dimensions are reduced, and focusing the analysis only on the relevant spatial region. Next, using mirroring (flipping) operations and rotations, the flipped hologram is re-oriented as the first one. Finally, rigid translations are applied to accurate align and centre the structures within the field of view. This alignment procedure is carried out manually to ensure that corresponding features overlap as precisely as possible and therefore minimize reconstruction artifacts related to misalignments. All the transformations applied to the holograms are identically performed on the corresponding reference hologram, preserving their spatial correspondence. This first image processing is represented in Fig. 4.10 applied to the NP-A1 sample.

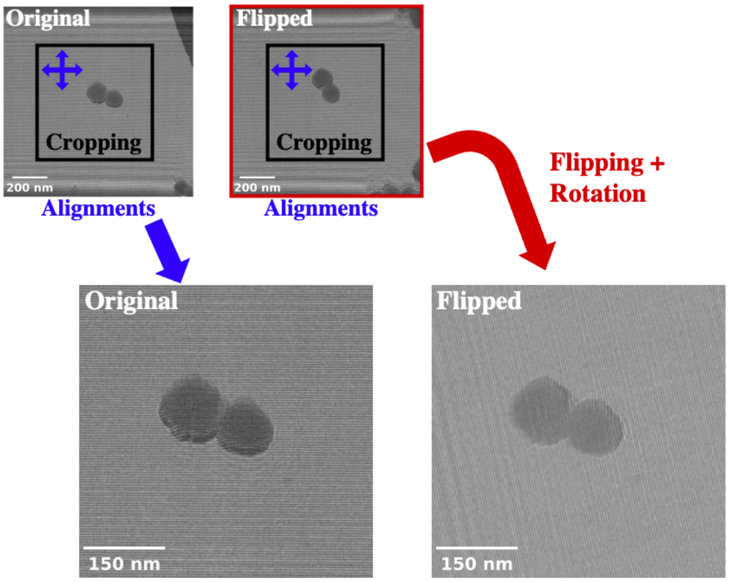

**Figure 4.10:** Cropping, alignment, rotation and flipping applied to the sample NP-A1

2. **Rebinning**:
To improve the robustness of the phase reconstruction and reduce both noise and computational load, a rebinning operation is applied on the holograms. Rebinning consists of resampling the image onto a coarser spatial grid, by grouping neighbouring pixels into larger bins. In this work, each new pixel is obtained by averaging the intensities of $r_b \times r_b$ adjacent pixels, where $r_b$ is the rebinning factor. As a result, the size of the image is reduced from $D$ to $D/r_b$, while the effective pixel size increases to ($p_{reb} = r_b\ p_{in}$). This operation corresponds to a local spatial averaging of electron intensity distribution and has multiple effects on the hologram. It reduces the spatial resolution and leads to a loss of fine structural details, but it significantly improves the signal-to-noise ratio (SNR), averaging out over multiple pixels. This SNR improvement is particularly relevant in electron holography, where, in general, the phase reconstruction is highly sensitive to noise and small intensity fluctuations. Therefore, rebinning enhances the stability and reliability of the subsequent reconstruction algorithm at the cost of a reduction in spatial resolution. Its effect is represented in Fig 4.11a, applied on the original hologram with $r_b = 2$ , the effects on the resolution are not visible with this number of pixels, but the image dimension halves while the pixel size doubles.

3. **Fourier Transform**:
The holograms are now ready for the first step of the reconstruction algorithm presented in Section 3.3.1. Their Fourier Transform is computed using the Fast Fourier Transform (FFT) algorithm and the corresponding diffractogram is obtained (Fig 4.11b). Cropping and rebinning have reduced the size of the image and thereby they decrease the computational cost of the FFT (smaller number of point to compute in Fourier space). In addition, rebinning acts as an effective low-pass filter, cutting off and attenuating high frequency noise components in the diffractogram. As a result, the Fourier spectrum becomes cleaner and easier to interpret,

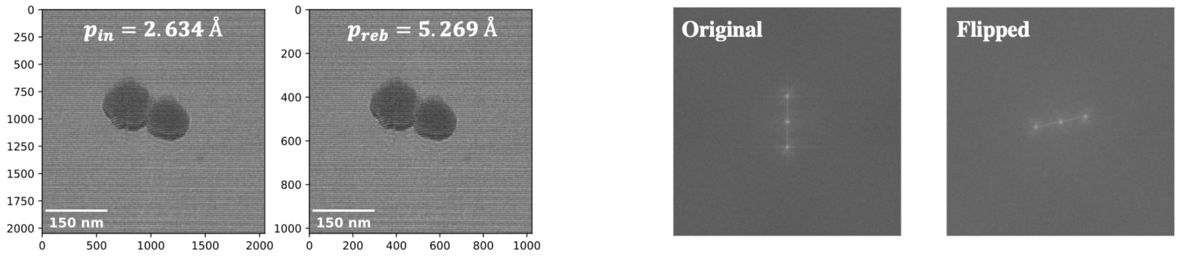

**(a)** **(b)**

**Figure 4.11:** (a) Rebinning effect on the original hologram. The effect in resolution are not visible in these images, but the number of pixels halves and the pixel size doubles (b) Fourier Transform of the two holograms. The points in the FT resides on a line perpendicular to the interference fringes.

allowing the holographic sidebands to be more reliably identified and isolated. It is also important to mention that reducing the Field of View (FoV) has a direct impact on the Fourier domain sampling (defined by the frequency resolution $\Delta k \sim \frac{1}{FoV}$): a smaller FoV leads to a larger spacing between adjacent k-points in Fourier space, shrinking the precision with which frequency components can be resolved. Therefore, while this trade-off improves signal-to-noise ratio and computational efficiency, excessive rebinning results in an irreversible loss of high-frequency information. This loss may degrade the fidelity of the reconstructed hologram by limiting the ability to resolve fine spatial features and increasing blurring in the reconstructed object.

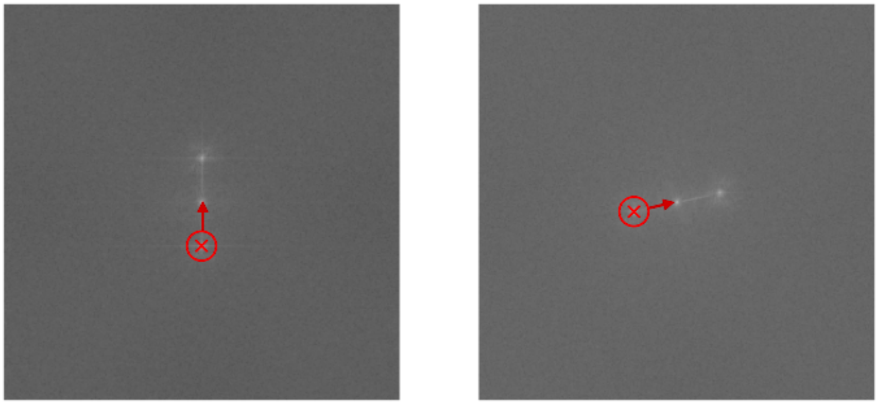

**Figure 4.12:** Selection of the sideband, masking with circular aperture (in this case of radius 38 px) and shifting to the centre. The red circle is the circular mask. The red arrow shows the shifting to the centre of the sideband

4. **Select, masking and centering the sideband**:
   At this point, one of the two sidebands can be selected from the Fourier spectrum by means of a numerical aperture and then shifted to the origin of the reciprocal space (Fig. 4.12). This operation isolate the interference term containing the object information, preparing the data for the inverse reconstruction. The choice of the mask geometry is crucial to determine the quality of the subsequent reconstruction. In particular, the radius of this window $r_w$ defines

the range of spatial frequencies retained in the inverse Fourier transform, effectively setting the bandwidth of the reconstruction. The mask operates as a low-pass filter: a smaller radius strongly suppresses high-frequency components, leading to a smoother and less noisy phase, but with a smaller spatial resolution, deleting fine details of the object. On the other hand, a larger radius preserves a larger range of spatial frequencies, improving the resolution but increasing the sensitivity to noise. Calling $d$ the distance between the centre of the sideband and the origin of the Fourier space (where the zero order direct peak is located), the mask radius must remain below $\frac{d}{2}$ to avoid overlap with the zero-order contribution. In practical electron holography, a more conservative choice is adopted, due to the finite extent of the spectral components and the presence of noise, and the ideal mask radius is commonly set approximately to $\frac{d}{3}$. This value constitutes a good compromise between conserve relevant spatial frequencies and suppressing unwanted spectral contributions. To explain better the behavior of the algorithm as a function of $r_w$, different reconstructed phase for this sample are reported Fig. 4.13 for 3 different window sizes. By observing the reconstructed phase, is evident that using a smaller aperture radius, the phase presents a reduced noise, but loosing high frequency details, which are better visible when larger aperture radii are employed. The third radius presented ($r_w = 55$ px) is essentially equal to $\frac{d}{2}$ and therefore undesired spectral contributions could enter in the phase. The best compromise is $r_w = \frac{d}{3} = 38$ px, preserving high frequency details and avoiding zero order contributions. The shape and the edge profile of the mask play an important role. A circular mask is generally implemented and its edge profile has important effect on the reconstruction. Sharp-edged masks introduce abrupt truncation in Fourier space, that can result in artifacts in the reconstructed image. These defects can be overcome by using smoother functions at the edges (Gaussian or sigmoid profiles), leading to improved continuity of the reconstructed phase and reduced edge artifacts. This masking procedure can be interpreted as a sort of regularization step in the inverse problem of holographic reconstruction, since it controls resolution, noise suppression and artifact minimization.

5. **Inverse Fourier Transform**:
After the masking and centering of the sideband, defining the range of spatial frequencies retained for the reconstruction, the inverse Fourier transform is performed using Inverse FFT algorithm. This operation reconstructs the complex wavefunction in real space, from which amplitude and phase distributions are extracted. The IFFT is applied on a finite grid, whose size can be selected during the reconstruction procedure. This choice defines the final reconstructed image dimension and can be seen as a cropping operation in Fourier domain to a square region before the inverse transform. This operation consists of a truncation of the Fourier spectrum, meaning that only a subset of the previously selected frequency components is retained. The spectral support is therefore further restricted, reducing beyond the effects of the circular mask applied during the sideband selection. From a physical perspective, this truncation further suppresses high-frequency components located near the edge of the sideband, leading to a smoother reconstructed phase and an improved robustness against noise. However, this happens again at the cost of reduced spatial resolution and loss of fine

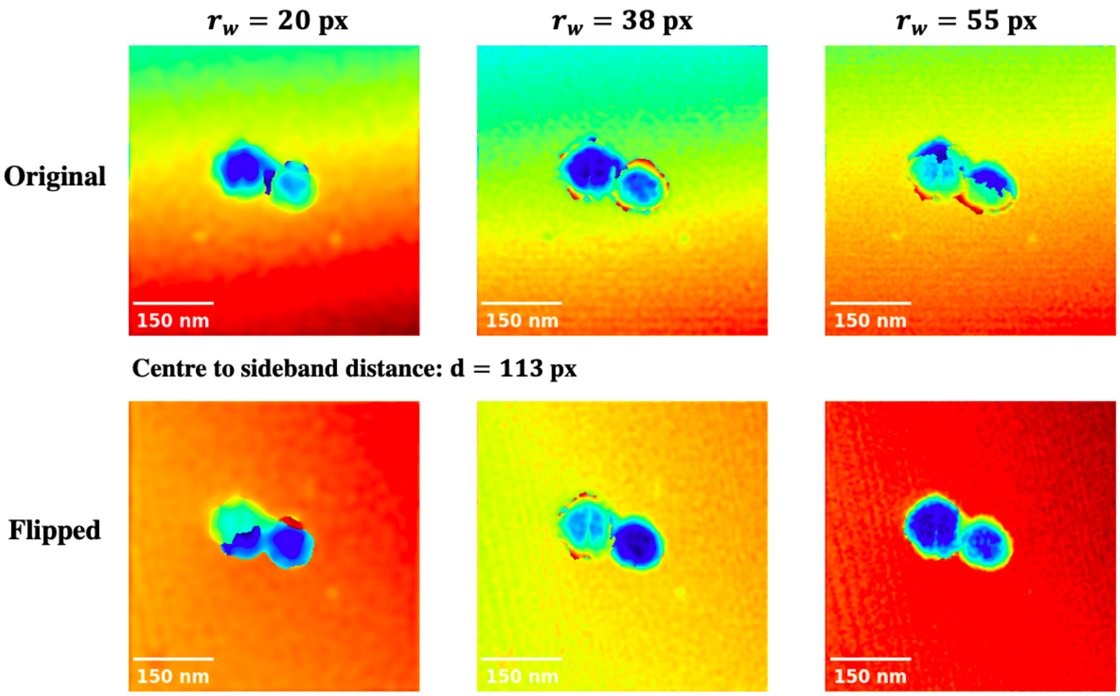

**Figure 4.13:** Different reconstructed unwrapped phase for NP-A1 sample ontained as a function of the radius of the. Results obtained after inverse Fourier transformation. Smaller is the aperture higher is the suppression for the high frequency components. All the images are reconstructed setting the final shape of the image at 256 px

structural details. Moreover the sharp boundaries introduced by this operation can introduce artifacts in the reconstructed images. This additional filtering, in this case, is combined with a modification in the sampling properties. Reducing the size in Fourier domain decreases the number of pixels in the reconstructed image, leading to a coarser spatial sampling, effectively increasing the pixes size. In particular, if the original hologram contains $D \times D$ pixels (of pixel size after rebinning $p_{reb}$) and the selected final shape, by means of Fourier cropping, is $D_f \times D_f$, the resulting final pixel size becomes $p_f = \frac{D}{D_f} p_{reb}$. This relation shows how the pixel size increases as the Fourier domain is reduced, resulting in a coarser spatial representation of the reconstructed image, with a smaller field of view. Therefore is evident how the parameter $D_f$ not only controls the computational cost of the inverse transform, but also directly affect the spatial sampling, effective resolution and extent of the reconstructed image. However, the effective spatial resolution $\delta x$ is mainly also controlled by the $r_w$, with $\delta x \sim \frac{1}{r_w}$. The two parameters $D_f$ and $r_w$ has a direct impact on the reconstructed image properties and work together and to avoid undersampling, which happens when the reconstructed pixel size is too large to represent the highest spatial frequencies and so is bigger than the effective spatial resolution. To be more accurate, the sampling condition in the reconstructed image needs to satisfy the Nyquist-Shannon criterion: $p_f \leq \frac{1}{2k_{max}}$, ensuring that at least two sampling points are available per smallest spatial period. The results of different aperture dimensions are reported in Fig...

### 6. Normalization with reference hologram and extraction of phase and amplitude

All the operations in the previous steps are always performed also on the references, that at this point, as decribed in Section 3.3.1, are used to normalize the complex quantities obtained from the inverse Fourier transform of the holograms. Then, phase and amplitude can be finally reconstructed and analyzed. The phases are treated with the unwrapping algorithm in order to delete the periodicity and, when necessary, they are also post-processed with smoothing techniques and with subtraction of polynomial background, to remove specific noise, defects and not related signals from other structures or sources. Then the electric and magnetic phase can be extracted using Eq. 3.7 and Eq. 3.8 and they can be studied to extract specific properties of materials The results are reported in Fig...

Finally, at this point, the reconstructed phase and the following extracted magnetic and electrostatic phases are reported for this couple of nanoparticles.

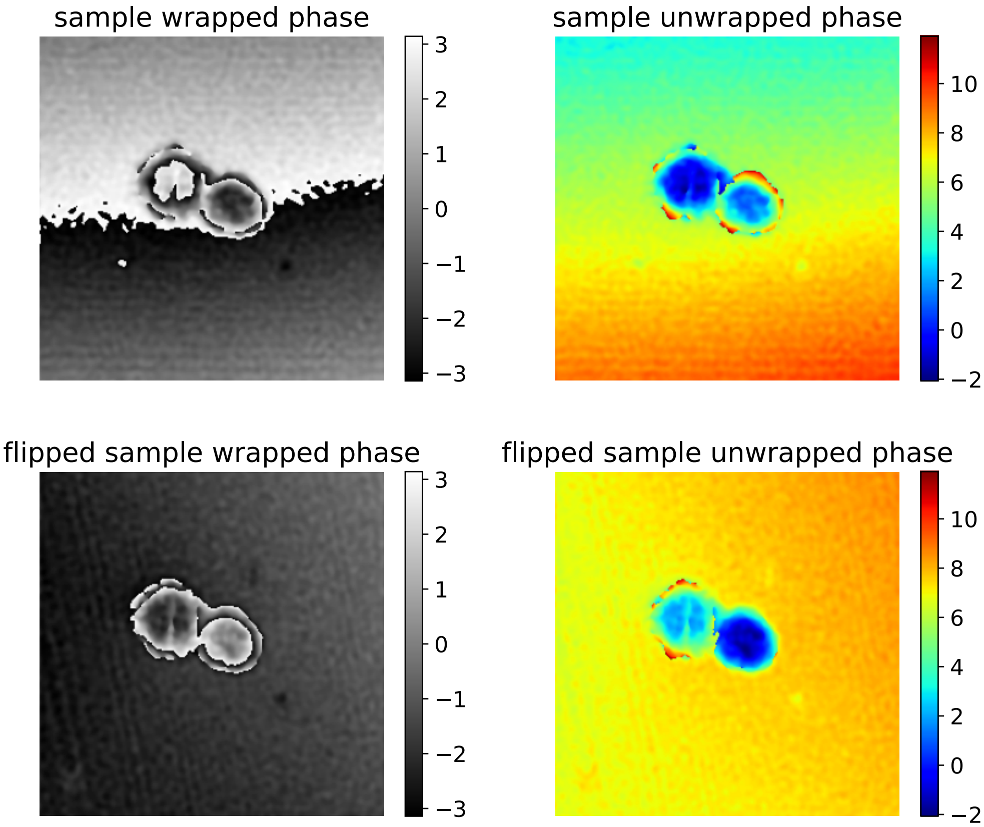

**Figure 4.14**

The magnetic and electrostatic contribution to the phase are the following and to enhance their behavior also their cosine (in this case amplificated are presented).

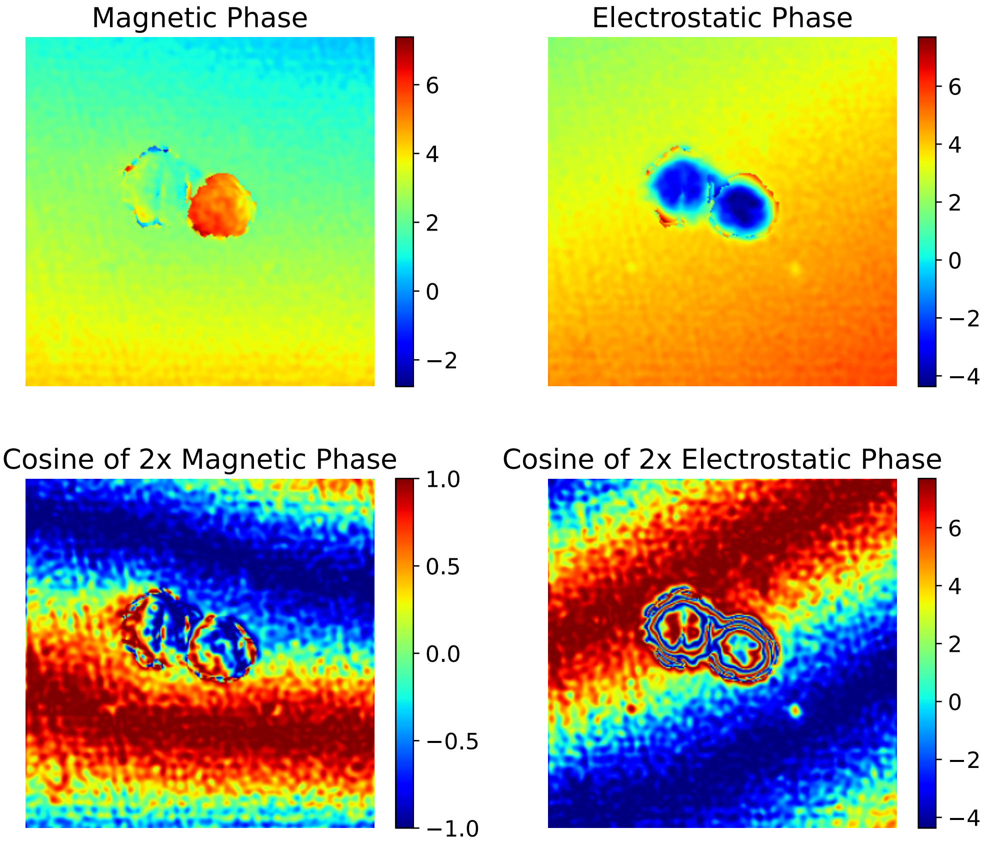
Magnetic Phase

Electrostatic Phase

Cosine of 2x Magnetic Phase

Cosine of 2x Electrostatic Phase

**Figure 4.15**

# Conclusions and perspectives

This work has investigated the application of phase microscopy to the study of Iron Cobalt magnetic nanoparticles and nanochains, combining a rigorous theoretical framework with numerical simulations and experimental analysis. Starting from the wave optical description of the electron, its phase is identified as the fundamental tool for probing the electromagnetic field at the nanoscale. Within this context, the magnetic behavior of the investigated nanostructures has been quantitatively characterized, enabling the extraction of their constitutive magnetic properties such as magnetic moment and magnetic flux. The resulting values have been consistent with expected values and, in good approximation, with what is reported in the literature. These results confirm the effectiveness of electron holography as a quantitative tool for nanoscale magnetism and demonstrate its capability to resolve signals at high spatial resolution.

The Transmission Electron Microscope has been fully described and understood, both from a theoretical and a practical perspective. Conventional TEM imaging has been integrated with phase techniques, with a special focus on off-axis electron holography. This method has been central to this thesis, starting from first principles –how electron waves interact with electric and magnetic potentials– all the way to its full experimental and computational implementation. Special attention has been given to the computational implementation of the phase retrieval algorithm, including a detailed presentation and study of each step needed for the reconstruction to succeed. Each step is critically analyzed, allowing the evaluation of uncertainties and limitations associated with this technique.

Overall, this work highlights how phase microscopy, and in particular off-axis electron holography, does represent a powerful and versatile approach for quantitative characterization of magnetic nanomaterials. At the same time, several aspects emerge as directions towards future improvements. The reconstrucion algorithm can be further refined by optimizing critical steps, such as hologram alignment, phase unwrapping and post processing of the reconstructed phase. The accuracy of uncertainty estimation also requires deeper investigation to ensure a fully reliable quantitative analysis.

On the experimental side, improving hologram quality and developing alternative strategies to isolate the magnetic phase contribution would be important. In particular, relying on turning over the sample has proven extremely demanding, especially in terms of reproducibility and precise realignment.

Further progress can also be achieved through improved and standardized deposition methods, enabling better control over the nanoparticle distribution and density on the grid and ensuring higher reproducibility. In addition, the integration of complementary magnetic sensitive techniques, such as Transport of Intensity Equation (TIE) and Differential Phase Contrast (DPC), would provide valuable cross-validation and useful comparisons.

To conclude, the results presented in this thesis contribute to the deeper understanding of the magnetic propertis of FeCoO nanostructures and demonstrate the significant potential of phase-based electron microscopy techniques for advanced nanomagnetic investigation. These methods, supported by robust theoretical modeling and computational analysis, represent a key tool for the future exploration of complex magnetic systems at the nanoscale.

# Bibliography

[1] Stephen Blundell. *Magnetism in Condensed Matter*. Oxford Master Series in Condensed Matter Physics. Oxford: Oxford University Press, 2001.

[2] David B. Williams and C. Barry Carter. *Transmission Electron Microscopy: A Textbook for Materials Science*. 2nd ed. Boston: Springer, 2009. ISBN: 9780387765006.

[3] Bawoke Mekuye and Birhanu Abera. "Nanomaterials: An overview of synthesis, classification, characterization, and applications". In: *Nano Select* 4.8 (2023), pp. 486–501. DOI: `https://doi.org/10.1002/nano.202300038`.

[4] Sudip Mukherjee et al. "Introduction to Magnetic Nanomaterials". In: *Magnetic Nanomaterials: Innovation for Cancer Theranostics*. IOP Publishing, 2020. Chap. 1.

[5] Georgy Mikhaylov et al. "Theranostic Applications of an Ultra-Sensitive T1 and T2 Magnetic Resonance Contrast Agent Based on Cobalt Ferrite Spinel Nanoparticles". In: *Cancers* 14.16 (2022). DOI: `10.3390/cancers14164026`.

[6] A. Omelyanchik et al. "Shell Thickness-Dependent Anisotropy in CoFe2O4@NiFe2O4 Core/Shell Nanoparticles for Magnetic Heating". In: *IEEE Transactions on Magnetics* 62.2 (2026), pp. 1–6. DOI: `10.1109/TMAG.2025.3646767`.

[7] Y. Chen and A. El-Ghazaly. "Self-Assembly of Magnetic Nanochains in an Intrinsic Magnetic Dipole Force-Dominated Regime". In: *Small* 19.7 (2023), e2205079. DOI: `10.1002/smll.202205079`.

[8] Jean Pierre Miranda Murillo et al. "Topochemical reduction of FeCo-oxide to FeCo-alloy nanosystems into a $SiO_2$ matrix". In: *Physical Chemistry Chemical Physics* 27 (2025), pp. 9504–9510. DOI: `10.1039/D5CP00305A`.

[9] Till Burkert et al. "Giant Magnetic Anisotropy in Tetragonal FeCo Alloys". In: *Phys. Rev. Lett.* 93 (2 2004), p. 027203. DOI: `10.1103/PhysRevLett.93.027203`.

[10] Xuefeng Zhang et al. "High-Magnetization FeCo Nanochains with Ultrathin Interfacial Gaps for Broadband Electromagnetic Wave Absorption at Gigahertz". In: *ACS Applied Materials & Interfaces* 8.5 (2016), pp. 3494–3498. DOI: `10.1021/acsami.5b12203`.

[11] Jie Yuan and Zhi-Quan Liu. "Flexible and self-assembly anisotropic FeCo nanochain-polymer composite films for highly stretchable magnetic device". In: *Composites Science and Technology* 164 (2018), pp. 8–16. ISSN: 0266-3538. DOI: `https://doi.org/10.1016/j.compscitech.2018.05.025`.

[12] Ludwig Reimer and Helmut Kohl. *Transmission Electron Microscopy: Physics of Image Formation*. 5th ed. New York: Springer, 2008. ISBN: 9780387402932.

[13] Deutsches Museum. *Replica of the First Electron Microscope by Ernst Ruska and Max Knoll*. Accessed: 2026-02-02. 1933.

[14] Louis de Broglie. "Recherches sur la théorie des quanta". In: *Annales de Physique* 10.3 (1925), pp. 22–128. DOI: `10.1051/anphys/192510030022`.

[15] M. Knoll and E. Ruska. "Das Elektronenmikroskop". In: *Zeitschrift für Physik* 78 (1932), pp. 318–339. DOI: `10.1007/BF01342199`.

[16] The Nobel Prize. *Press Release: The Nobel Prize in Physics 1986*. `https://www.nobelprize.org/prizes/physics/1986/press-release/`. Accessed: 2026-02-22. 1986.

[17] Market Growth Reports. *Transmission Electron Microscope (TEM) Market Size, Share, Growth and Industry Analysis*. Tech. rep. Report ID: 114699, accessed 2026-02-20. Market Growth Reports, 2025. URL: `https://www.marketgrowthreports.com/market-reports/transmission-electron-microscope-tem-market-114699`.

[18] JEOL Ltd. *Glossary of Electron Microscopy Terms*. Accessed: 2026-03-28. URL: `https://www.jeol.com/words/emterms/`.

[19] Duncan T. L. Alexander. *TEM Ray Diagrams - École Polytechnique Fédérale de Lausanne (EPFL)*. Electron Spectrometry and Microscopy Laboratory (LSME), EPFL. 2025. URL: `https://www.epfl.ch/labs/lsme/tem-ray-diagrams/` (visited on 03/03/2026).

[20] Ray F. Egerton, Peng Li, and Marek Malac. "Radiation damage in the TEM and SEM". In: *Micron* 35.6 (2004), pp. 399–409. DOI: `10.1016/j.micron.2004.02.003`.

[21] David B. Williams and C. Barry Carter, eds. *Transmission Electron Microscopy: Diffraction, Imaging, and Spectrometry*. Cham, Switzerland: Springer International Publishing, 2016. DOI: `10.1007/978-3-319-26651-0`.

[22] John C. H. Spence. *High-Resolution Electron Microscopy*. 4th ed. Oxford, UK: Oxford University Press, 2013. ISBN: 9780199668632.

[23] Hans Lichte and Michael Lehmann. "Electron holography—basics and applications". In: *Reports on Progress in Physics* 71.1 (2007). DOI: `10.1088/0034-4885/71/1/016102`.

[24] D.L. Misell. "Chapter Four - The phase problem in electron microscopy". In: *Advances in Imaging and Electron Physics*. Ed. by Martin Hÿtch and Peter W. Hawkes. Vol. 225. Advances in Imaging and Electron Physics. Elsevier, 2023, pp. 163–262. DOI: `https://doi.org/10.1016/bs.aiep.2022.12.004`.

[25] Giulio Pozzi, ed. *Particles and Waves in Electron Optics and Microscopy*. Vol. 194. Advances in Imaging and Electron Physics. Academic Press, 2016. ISBN: 9780128045930.

[26] Takeshi Kasama, Rafal E. Dunin-Borkowski, and Marco Beleggia. "Electron Holography of Magnetic Materials". In: *Holography - Different Fields of Application*. Ed. by Freddy Alberto Monroy Ramírez. InTech, 2011, pp. 53–80. ISBN: 978-953-307-635-5. DOI: `10.5772/22366`.

[27] W. Ehrenberg and R. E. Siday. “The Refractive Index in Electron Optics and the Principles of Dynamics”. In: *Proceedings of the Physical Society. Section B* 62.1 (1949), pp. 8–21. DOI: `10.1088/0370-1301/62/1/303`.

[28] Yakir Aharonov and David Bohm. “Significance of Electromagnetic Potentials in the Quantum Theory”. In: *Physical Review* 115.3 (1959), pp. 485–491. DOI: `10.1103/PhysRev.115.485`.

[29] R. G. Chambers. “Shift of an Electron Interference Pattern by Enclosed Magnetic Flux”. In: *Physical Review Letters* 5.1 (1960), pp. 3–5. DOI: `10.1103/PhysRevLett.5.3`.

[30] Akira Tonomura. “Applications of Electron Holography”. In: *Reviews of Modern Physics* 59.3 (1987), pp. 639–669. DOI: `10.1103/RevModPhys.59.639`.

[31] M. De Graef, N. T. Nuhfer, and M. R. McCartney. “Phase contrast of spherical magnetic particles”. In: *Journal of Microscopy* 194.1 (1999), pp. 84–94. DOI: `https://doi.org/10.1111/jmi.1999.194.1.84`.

[32] Alexander Omelyanchik et al. “High-Moment FeCo Magnetic Nanoparticles Obtained by Topochemical H2 Reduction of Co-Ferrites”. In: *Applied Sciences* 12.4 (2022). DOI: `10.3390/app12041899`.

[33] Binil Kandapallil et al. “Synthesis of high magnetization Fe and FeCo nanoparticles by high temperature chemical reduction”. In: *Journal of Magnetism and Magnetic Materials* 378 (2015), pp. 535–538. DOI: `https://doi.org/10.1016/j.jmmm.2014.11.074`.

[34] Qi-Liang Ye, Hideo Yoshikawa, and Kazunari Awaga. “Magnetic and Optical Properties of Submicron-Size Hollow Spheres”. In: *Materials* 3.2 (2010), pp. 1244–1268. DOI: `10.3390/ma3021244`.

[35] Pedro Tartaj et al. “The preparation of magnetic nanoparticles for applications in biomedicine”. In: *Journal of Physics D: Applied Physics* 36.13 (2003), R182–R197. DOI: `10.1088/0022-3727/36/13/202`.

[36] C. Phatak et al. “On the magnetostatics of chains of magnetic nanoparticles”. In: *Journal of Magnetism and Magnetic Materials* 323.22 (2011), pp. 2912–2922. DOI: `https://doi.org/10.1016/j.jmmm.2011.06.058`.

[37] Gabriel Sanchez-Santolino et al. “Phase Imaging Methods in the Scanning Transmission Electron Microscope”. In: *Nano Letters* 25 (2025), pp. 10709–10721. DOI: `10.1021/acs.nanolett.4c06697`.

[38] Marco Beleggia et al. “On the transport of intensity technique for phase retrieval”. In: *Ultramicroscopy* 102.1 (2004), pp. 37–49. DOI: `10.1016/j.ultramic.2004.08.002`.

[39] J. N. Chapman. “The application of iterative techniques to the investigation of strong phase objects in the electron microscope”. In: *The Philosophical Magazine: A Journal of Theoretical Experimental and Applied Physics* 32.3 (1975), pp. 527–540. DOI: `10.1080/14786437508220877`.

[40] J. R. Fienup. “Phase retrieval algorithms: a comparison”. In: *Appl. Opt.* 21.15 (1982), pp. 2758–2769. DOI: `10.1364/AO.21.002758`.

[41] Andrew M. Maiden and John M. Rodenburg. “An improved ptychographical phase retrieval algorithm for diffractive imaging”. In: *Ultramicroscopy* 109.10 (2009), pp. 1256–1262. DOI: `https://doi.org/10.1016/j.ultramic.2009.05.012`.

[42] Peter Ercius et al. “Electron Tomography: A Three-Dimensional Analytic Tool for Hard and Soft Materials Research”. In: *Advanced Materials* 27.38 (2015), pp. 5638–5663. DOI: `https://doi.org/10.1002/adma.201501015`.

[43] Dennis Gabor. “A New Microscopic Principle”. In: *Nature* 161 (1948), pp. 777–778. DOI: `10.1038/161777a0`.

[44] Emmett N. Leith and Juris Upatnieks. “Reconstructed Wavefronts and Communication Theory”. In: *Journal of the Optical Society of America* 52.10 (1962), pp. 1123–1130. DOI: `10.1364/JOSA.52.001123`.

[45] G. Möllenstedt and H. Wahl. “Elektronenholographie und Rekonstruktion mit Laserlicht”. In: *Naturwissenschaften* 55.7 (1968), pp. 340–341. DOI: `10.1007/BF00600454`.

[46] Akira Tonomura. “Development of Electron Holography and Its Applications to Fundamental Problems in Physics”. In: *Japanese Journal of Applied Physics* 47.1 (2008), pp. 11–18. URL: `https://www.jsap.or.jp/jsapi/Pdf/Number18/04_JJAP.pdf`.

[47] The Nobel Prize. *Press Release: The Nobel Prize in Physics 1971*. `https://www.nobelprize.org/prizes/physics/1971/summary/`. Accessed: 2026-03-22. 1971.

[48] Akira Tonomura et al. “Observation of Aharonov-Bohm Effect by Electron Holography”. In: *Phys. Rev. Lett.* 48 (21 1982), pp. 1443–1446. DOI: `10.1103/PhysRevLett.48.1443`.

[49] Paul A. Midgley and Rafal E. Dunin-Borkowski. “Electron tomography and holography in materials science”. In: *Nature Materials* 8.4 (2009), pp. 271–280. DOI: `10.1038/nmat2406`.

[50] J. E. Bonevich et al. “Electron holography observation of vortex lattices in a superconductor”. In: *Phys. Rev. Lett.* 70 (19 1993), pp. 2952–2955. DOI: `10.1103/PhysRevLett.70.2952`.

[51] G. Möllenstedt and H. Dūker. “Beobachtungen und Messungen an Biprisma-Interferenzen mit Elektronenwellen”. In: *Zeitschrift fūr Physik* 145.4 (1956), pp. 377–397. DOI: `10.1007/BF01389199`.

[52] Kohji Harada. “Interference and interferometry in electron holography”. In: *Microscopy* 70.1 (2021), pp. 3–16. DOI: `10.1093/jmicro/dfaa033`.

[53] Jo Verbeeck, Giovanni Bertoni, and Hannes Lichte. “A holographic biprism as a perfect energy filter?” In: *Ultramicroscopy* 111.7 (2011). Special Issue: J. Spence’s 65th birthday, pp. 887–893. DOI: `https://doi.org/10.1016/j.ultramic.2011.01.042`.

[54] Dennis C. Ghiglia and Louis A. Romero. “Robust two-dimensional weighted and unweighted phase unwrapping that uses fast transforms and iterative methods”. In: *J. Opt. Soc. Am. A* 11.1 (1994), pp. 107–117. DOI: `10.1364/JOSAA.11.000107`.

[55] András Kovács and Rafal E. Dunin-Borkowski. "Magnetic Imaging of Nanostructures Using Off-Axis Electron Holography". In: *Handbook of Magnetic Materials*. Ed. by Ekkes H. Brück. Vol. 27. Elsevier, 2018, pp. 59–153. DOI: `10.1016/bs.hmm.2018.09.001`.

[56] Etienne Snoeck and Christophe Gatel. "Magnetic Mapping Using Electron Holography". In: *Transmission Electron Microscopy in Micro-Nanoelectronics*. Ed. by Alain Claverie. Berlin, Heidelberg: Springer, 2008. Chap. 5, pp. 107–133.